Fourier Pipeflow Manipulation for Thermal Energy Systems

BY

Nawaf Talal Mohammed Salem

A THESIS SUBMITTED IN PARTIAL FULFILMENT OF THE REQUIREMENTS FOR THE DEGREE OF

MASTER OF SCIENCE

DEPARTMENT OF MECHANICAL ENGINEERING

UNIVERSITY OF ALBERTA

ABSTRACT

This dissertation numerically evaluates the performance of targeted wall-shape pipe inserts on reducing heat convection and frictional drag of turbulent pipeflow at a range of Reynolds numbers, $Re = 2.5 \times 10^4 - 7.5 \times 10^4$. The wall modifications are constructed to closely follow three azimuthal Fourier modes corresponding to $m = 3$ (Case I), 15 (Case II), and $3 + 15$ (Case III). The implementation of these pipe-inserts generate flow features that can render significant improvements to the efficiency of subsurface thermal processes, including extraction and harvesting of geothermal energy. First, thermal response is investigated by characterizing mean flow and convective heat transfer features downstream of the pipe-inserts at $Re = 7.5 \times 10^4$. Particularly, the results exhibit a maximum reduction of $\sim 9\%$ in near-wall heat transfer for Case II and Case III, compared to a smooth pipe. The fully-developed thermal condition is recovered at an axial location of $x/D = 40$ from the perturbation, where D is the pipe diameter. Further, a significant attenuation in skin-frictional drag is observed, hinting at maximum decrease of 17.4% and 16.5% for Case II and Case III, respectively. At $x = 2D - 10D$ following the inserts, the maximum averaged contractions in near-wall heat transfer and frictional drag are depicted for Case II, corresponding to 3.4% and 5.0%, respectively. The wall modification of Case I results in a relatively minor impact on convective heat transfer and frictional drag, before returning to fully-recovered state. Reynolds number implications suggest increasing reductions of near-wall convective heat transfer and frictional drag with decreasing Re. The maximum reductions of $\sim 10.5\%$ and $\sim 20.5\%$ in near-wall convective heat transfer and frictional drag are achieved at the lowest Reynolds number of 2.5×10^4, indicating averaged reductions of 5.7% and 8.3% within $x = 2D - 10D$, respectively. Increasing Reynolds number delays heat transfer recovery, which depicts an asymptotic trend for $Re \geq 5.0 \times 10^4$. This research found that targeted wall-shape pipe inserts contribute to mitigation of near-wall convective heat transfer with a decrease in frictional drag. These contributions hint at extensive enhancements to the efficiency of energy extraction and transportation in subsurface thermal applications.

PREFACE

The results of Chapter 4 are under-review for publication in the Journal of *Applied Thermal Engineering* with the following citation:

Salem, N., Tarokh, A., Hemmati, A. (2022). A novel pipeflow manipulation technique for subsurface thermal applications. *Applied Thermal Engineering*.

The results of Chapter 5 are under-review for publication in the Journal of *Physics of Fluids* with the following citation:

Salem, N., Tarokh, A., Hemmati, A. (2022). Reynolds number effects on heat transfer and frictional drag implications of turbulent pipeflow past targeted wall shapes. *Physics of Fluids*.

All the simulations, data curation, and results discussions presented in this dissertation were completed by Nawaf Salem under the supervision of Drs. Arman Hemmati and Ali Tarokh. Compute Canada resources were utilized to run the simulations.

To Mom and Dad, my sister and my wife,

for your love and continual support

ACKNOWLEDGEMENTS

Contents

List of Tables

List of Figures

LIST OF ABBREVIATIONS, SYMBOLS, AND

NOMENCLATURE

Latin Symbols

D	diameter
R	radius
x	axial location
r	radial direction
θ	azimuthal angle
r^+	dimensionless radial distance
A	cross-sectional area
Re	Reynolds number
Re_τ	friction Reynolds number
k	turbulence kinetic energy
P_k	turbulence kinetic energy production
I	turbulence intensity
U_b	bulk velocity in far downstream region
U_∞	inlet bulk velocity of smooth-wall pipe
U_{CL}	centerline velocity magnitude
u_τ	bulk inlet friction velocity
$\overline{U_x}$	Cylindrical axial (x-wise) velocity component
$\overline{U_r}$	Cylindrical radial (r-wise) velocity component
$\overline{U_\theta}$	Cylindrical azimuthal (θ-wise) velocity component
$\overline{u'_x u'_r}$	Reynolds shear stress component
$\overline{u'^2_x}$	Reynolds normal stress component
$\overline{p}$	pressure

C_f	skin friction coefficient
$\overline{T}$	fluid Temperature
$\overline{T_w}$	wall Temperature
$\overline{T_b}$	bulk fluid Temperature
T_τ	friction Temperature
h	convective heat transfer coefficient
c_p	specific heat capacity at constant pressure
k_f	fluid thermal conductivity
q	wall heat flux
Nu	Nusselt number
Pr	Prandtl number
Pr	turbulent Prandtl number
L_r	recovery length
L_p	axial position of $\overline{U_x}$ peak
L_{pipe}	total pipe length
m	Fourier mode number
a_m	perturbation amplitude
c	characteristic length scale
t	time
T_p	averaging time period

Greek Symbols

δ_o	Boundary layer thickness
ε	Turbulent kinetic energy dissipation rate
ω	Turbulence specific dissipation rate

τ	Stress tensor
τ_w	Wall Shear Stress
ρ	density
μ	dynamic viscosity
ν	kinematic viscosity

Other Symbols

∇	gradient operator
$\overline{\square}$	mean (time-averaged)
∂	partial derivative
$\square \cdot \square$	dot product
Δ	difference
$\approx$	approximately
Σ	summation
$\propto$	proportional to

Abbreviations

2D	Two Dimensional
3D	Three Dimensional
CFD	Computational Fluid Dynamics
FVM	Finite Volume Method
DNS	Direct Numerical Simulation
LES	Large Eddy Simulation
RANS	Reynolds Averaged Navier Stokes

SST	Shear Stress Transport
PIV	Particle Image Velocimetry
LSMs	Large-Scale Motions
VLSMs	Very-Large-Scale Motions
SIMPLE	Semi-Implicit Method for Pressure Linked Equations

Chapter 1

INTRODUCTION

Turbulent pipe flow response and recovery to various disturbances, i.e., wall variations, is a classical problem in fluid mechanics (Smits et al., 1979; Durst and Wang, 1989; Yamagata et al., 2014; Smits et al., 2019; Goswami and Hemmati, 2020, 2021). These features can be utilized to manipulate the flow in transport of fluid and energy products towards lowering frictional drag and heat losses. This study quantitatively examines the capacity of distinct wall-shape pipe-inserts to suppress near-wall heat convection and reduce frictional drag in turbulent pipe flow at a range of Reynolds numbers. The pipe-wall modifications are created to closely follow certain azimuthal Fourier modes, which Masoumifar et al. (2021a,b) proved to have significant flow manipulation capabilities. This work establishes on the experimental and numerical findings of Van Buren et al. (2017) and Masoumifar et al. (2021a,b) on flow response and recovery of turbulent pipe flow encumbered by targeted pipe-inserts.

1.1   Motivation

The growing world population and global economy procure to a substantial rise in global energy demand (Johansson and Goldemberg, 2002). Currently, this demand is primarily satisfied by non-renewable energy resources, i.e., 78.3% fossil fuels and 2.5% neclear, while the contribution of renewable energies is approximately 19.2% (Sawin et al., 2016). The utilization of fossil

fuels leads to significant greenhouse gas emissions (GHG), which is a leading cause for emerging ecological issues, globally referred to as climate change (Johansson and Goldemberg, 2002; Wolf et al., 2016). For example, heating processes of natural gas in oil-sand industry accounts for 11% of Canada's national GHG emissions (Hu et al., 2022). Further, consumption of hydrocarbons contributes to air and water pollution, consequently harming human health, damaging aquatic ecosystems, and threatening the existence of wildlife (Günther and Hellmann, 2017; Soltani et al., 2019). These escalating concerns on the detrimental impacts of fossil fuels have sparked a global initiative for energy transition towards sustainable renewable energy systems at competitive costs (Garrett-Peltier, 2017). The renewable energy sector is rapidly growing, and it is predicted to account for 40% of the global energy supply by 2040 (Mead, 2017). Therefore, technological advancements in renewable energy are expected to emerge in next decades, which enable meeting future energy demand. This underlines the significance of exploring sustainable and ecologically-friendly renewable energy sources.

Geothermal reserves are of great interest for sustainable renewable energy harvesting. Geothermal energy harvesting works on the basis of harnessing thermal energy stored underground (Bayer et al., 2013). Due to the presence of a massive thermal storehouse of molten magma in the earth core, it continually conveys thermal energy to the outer crust (Elders and Moore, 2016). According to the assessment of WEC (2007), the overall obtainable geothermal energy is 1.5×10^{21} kWh. It should be noted that the current global energy demand is 7.5×10^{14} kWh, which can be sustained for 2000 years by exploiting only 0.1% of the available geothermal energy (Bertani, 2012). Geothermal energy systems can be employed for electricity production and/or direct use, depending on the extracted energy (DiPippo and Renner, 2014). Convectional geothermal resources, known as hydrothermal systems, are geologically limited to locations that exhibit high thermal gradients and substantial amounts of hot groundwater (Xu et al., 2015). These constraints have led to the evolution of enhanced geothermal systems (EGS), which are characterized as geographically-abundant geothermal reserves. EGS utilizes fracturing to extract commercial-scale thermal energy from low-permeability and/or low-porosity geothermal reserves (Tester et al., 2006). A typical

2
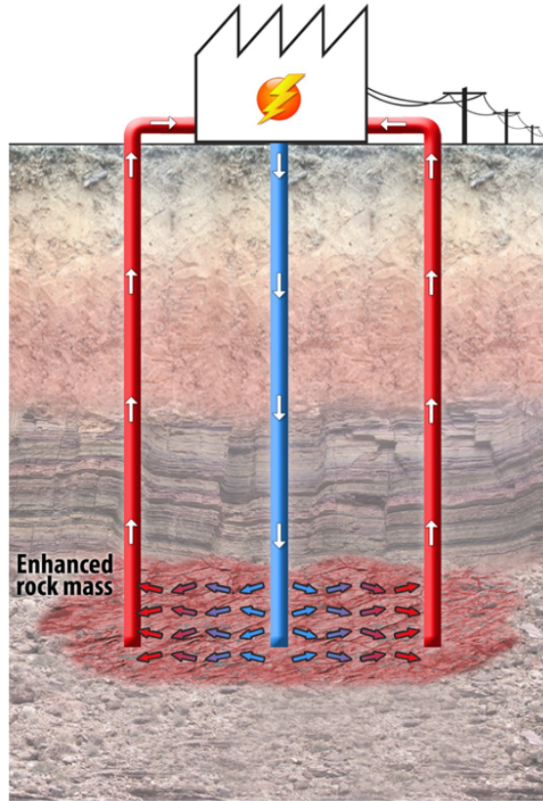
Figure 1.1: Schematic representation of a typical enhanced geothermal system. Reproduced from Johnston et al. (2011) with permission from Springer Nature.

EGS is constrcuted by installing one or multiple wells into the impermeable geothermal reservoir and injecting pressurized water to create fractures (enhancing reservoir permeability) (Xu et al., 2015; Kumari and Ranjith, 2019). The injected fluid gradually absorbs heat from subsurface highly-heated dry rocks. The heated fluid is sequentially extracted to surface through a production well (see Figure 1.1).

Geothermal systems have the largest capacity factor among various conventional and alternative sources of energy. However, development of global-scale geothermal energy harvesting systems faces many technological challenges. A major challenge is the existence of significant heat losses to the ground rock formations in the extraction processes through production wells (Phuoc et al., 2019; Xu et al., 2015). Heat losses to ground rock formations substantially affect the efficiency of geothermal systems and impedes their development as a major alternative source of energy. It is essential to recognize that heat losses to ground rock formations appear to evolve in

various thermal systems, including recovery processes of thermal energy from depleted oil sands reservoirs. Particularly, enhanced oil recovery involves injecting steam at elevated temperatures (above 200 °C) to heat the bitumen and lower its viscosity, thus facilitating the bitumen mobilization towards the production well (Wei et al., 2022). This oil extraction process is conventionally referred to as steam-assisted gravity drainage (SAGD). Examinations of SAGD operations revealed that approximately 2/3 of the injected thermal energy is stored by the reservoir rocks, which hints at the feasibility of recovering this thermal energy after the SAGD process is completed (Wang, 2021). Recovery of this thermal energy can be targeted to offset GHG emissions associated with SAGD processes. However, this process is significantly impacted by the existing deficiency related to heat losses. This technological issue has motivated us to introduce a novel passive flow manipulation technique with apparent operational benefits in thermal systems.

The challenges outlined thus far hint at the need for (1) attenuating near-wall convective heat transfer that impedes heat losses to ground rock formations in subsurface thermal systems and (2) lowering skin-friction drag, which results in reduced pumping power requirement. These multiple operational benefits could enhance the capacity of subsurface thermal systems, e.g., geothermal applications and energy recovery operations from depleted oil sands reservoirs.

This dissertation targets the manipulation of turbulent pipeflow and its convective heat transfer by implementing three-dimensional (3D) variations in pipe-wall shape. The pipe-wall modifications were designed to target certain Fourier modes, the details of which are provided in Section 1.2.

1.2 Pipe-Inserts

The newly introduced pipe-inserts incorporate 3D wall shape variations that resemble targeted azimuthal Fourier modes in wall-bounded turbulence (see Figures 1.2, 1.3, and 1.4). Three azimuthal Fourier modes were selected that exhibited the most energetic flow features, particularly $m = 3$ (Case I), $m = 15$ (Case II), and $m = 3 + 15$ (Case III). As stated by Van Buren et al. (2017); Prandtl
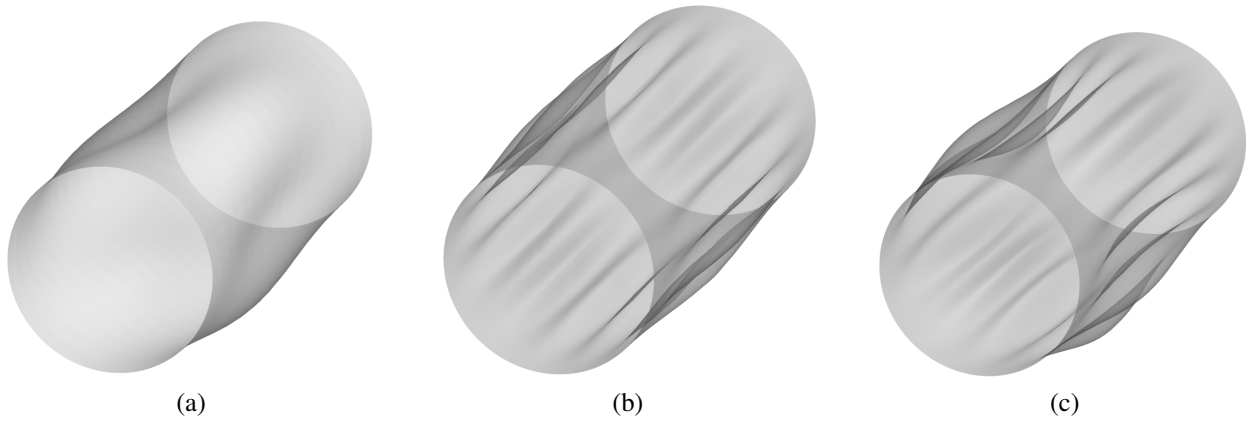
Figure 1.2: Scematics illustrations of Fourier pipe-inserts, (a) $m = 3$, (b) $m = 15$, and (c) $m = 3 + 15$.
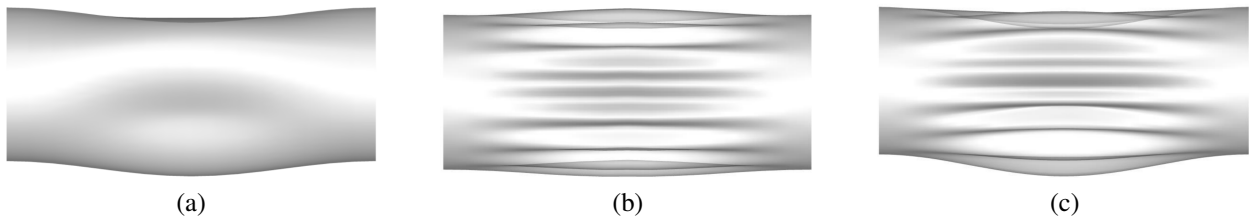
Figure 1.3: Side-view representation of Fourier pipe-inserts, (a) $m = 3$, (b) $m = 15$, and (c) $m = 3 + 15$.
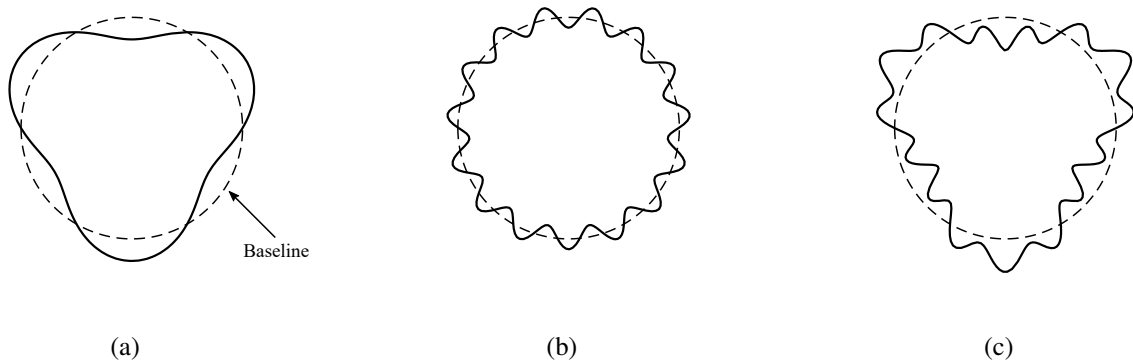
Figure 1.4: Schematics of the pipe-insert cross-sectional shapes at $x/D = 0$: (a) $m = 3$ (Case I), (b) $m = 15$ (Case II), (c) $m = 3 + 15$ (Case III).

(1952); Perkins (1970); Anderson et al. (2015), the targeted pipe-inserts have the capacity to substantially manipulate pipeflow dynamics by invoking spanwise gradients of Reynolds stresses. The

experiments of Van Buren et al. (2017) and simulations of Masoumifar et al. (2021a,b) shared that targeted pipe-wall modifications lead to deceleration and acceleration of mean flow in the near-wall and core flow regions, respectively. Further, these wall geometries suppress and transport turbulence away from the wall. The evolution of low-momentum flow in the near-wall region is proven to manipulate the flow towards reducing near-wall convective heat transfer and frictional drag (Castellanos et al., 2022; Schoppa and Hussain, 1998; Cheng et al., 2021; Whalley and Choi, 2014; Du et al., 2002). In addition, Smits et al. (2019) proposed that implementing abrupt wall perturbations can generate extended zones of lower frictional drag and convective heat transfer in the downstream wake, by conveying concentrated levels of Reynolds stresses away from the wall. The present study examines the feasibility of generating extended downstream region of reduced convective heat transfer, along with lower frictional drag, by implementing pipe-inserts with targeted wall-shapes.

Targeted wall modifications were implemented in the computational domain by placing pipe-inserts with an axial length of $4D$, where D is the pipe diameter, in the middle of a smooth-pipe following the experimental and numerical setups of Van Buren et al. (2017); Masoumifar et al. (2021a,b). Schematics of the maximum changes in cross-sectional shape of Fourier inserts are provided in Figure 1.4. The perturbation amplitude (a_m) translated evenly along the streamwise (axial) direction, following a sinusoidal function. The wall corrugation was mathematically formulated as:

$$r(\theta, m, x) = \frac{D}{2}\left[1 + \frac{\cos(\frac{\pi x}{2D}) + 1}{2}\sum_m a_m \sin(m\theta)\right]. \tag{1.1}$$

Here, r represents the radial distance, m is the Fourier mode, $\theta \in [0, 2\pi]$ symbolizes the azimuthal angle, and $x \in [-2D, 2D]$ denotes the axial (streamwise) location. The perturbation amplitude was $a_{m_1} = 0.2$ for Case I, $a_{m_2} = 0.1$ for Case II, and $a_{m_3} \in \{0.2, 0.1\}$ for Case III.

The average displacement angle of pipe wall with axial location was $2.8°$ for Case I and $1.4°$ for Case II. The maximum height (h) of the targeted geometries was $0.1D$ for Case I, $0.05D$ for Case II, and $0.15D$ for Case III. The change in cross-sectional area of perturbations is fully described as:

$$\Delta A = \frac{1}{2} \sum_m (\frac{2a_m}{D})^2,$$

(1.2)

with a maximum variation of 2% for Case I, 0.5% for Case II, and 2.5% for Case III (Van Buren et al., 2017).

1.3   Research Objectives

The main objective of this study is to evaluate the capability of targeted wall-shape pipe-inserts on favorably manipulating turbulent pipeflow and convective heat transfer characteristics at a range of Reynolds numbers, $Re = 2.5 \times 10^4 - 7.5 \times 10^4$. In particular, the research objectives:

1. Examine the thermal response of turbulent pipe flow past targeted wall-shape pipe-inserts.

2. Determine and characterize the recovery behaviour of convective heat transfer disturbed by targeted wall-shapes.

3. Evaluate the performance of targeted pipe-inserts in reducing near-wall convective heat transfer and frictional wall drag.

4. Investigate the implications of bulk Reynolds number on the performance of targeted pipe-wall perturbations.

1.4   Novelty

This thesis is the first of its kind to evaluate the thermal response and recovery of pipe flow impeded by targeted wall-shape pipe-inserts. Further, it addresses a knowledge gap on characterizing the performance of these pipe-inserts at a range of Reynolds numbers in concurrently minimizing heat losses and frictional drag. The outcomes presented in this thesis enrich our knowledge in thermal sciences and engineering, and it proposes the implementation of a particular technique to lower energy losses in subsurface thermal systems.

1.5   Structure of the Thesis

This dissertation begins with a literature review in Chapter 2, which delineates fundamental concepts in heat transfer and fluid dynamics. Chapter 2 also presents a concise review of fundamental principles of forced convection in turbulent flows and turbulence modeling. Further, Chapter 2 includes a through review on the existing literature on flow and thermal responses of turbulent flows with modified wall geometries. A detailed elucidation of research methodology and numerical setup, including domain sensitivity analysis, grid quality study, and validations, are outlined in Chapter 3. Chapter 4 elaborates the implications of Fourier pipe-inserts on convective heat transfer and frictional drag in turbulent pipe flow. Chapter 5 presents an extensive examination of thermal response and recovery at a range of Reynolds numbers between 2.5×10^4 and 7.5×10^4. The main conclusions are presented in Chapter 6 along with a discussion of unexplored research topics for future expansions of this dissertation.

Chapter 2

BACKGROUND

This dissertation employs principles, methods, and tools of computational fluid dynamics to examine the impacts of targeted pipe-inserts on manipulating convective heat transfer and frictional drag in turbulent pipe flow. Therefore, a brief discussion on fundamental principles in heat transfer, fluid mechanics, and turbulence modeling is essential for the theoretical background of this study. This chapter further provides a comprehensive literature review on flow manipulation techniques that strive to output favourable heat transfer and low-drag dynamics. This lays the state of literature for the current study.

2.1 Fundamentals of Heat Transfer

Heat transfer is an engineering science concerning thermal energy transfer between physical bodies solely by the virtue of spacial temperature gradients. Kakac et al. (1995) described heat as an energy form in transit across the physical boundaries of a system, where temperature gradient is the driving mechanism for heat propagation. In normal conditions, heat flows in the direction of negative temperature gradient, meaning from higher to lower temperatures.

There are three main modes by which heat is conveyed in an energy conversion system: conduction, convection, and radiation (Naterer, 2018). Conduction is the heat transfer mechanism associated with molecular motions. In other words, heat conduction is the transfer of molecular kinetic

energy from more vibrating (energetic) molecules in a high-temperature zone through molecular collisions to less energetic molecules in a low-temperature zone. Radiation is heat transfer process associated with emission and absorption of electromagnetic waves. All materials (solids, gases, and liquids) radiate heat by the virtue of their temperature. They also have the capability to absorb this energy. Further, radiation can propagate through vacuum, while heat conduction and convection require a physical medium. With liquids and gases, thermal energy can also be conveyed by the bulk flow motion in the presence of a macroscopic fluid movement. Convection is defined as the heat transfer mechanism that combines heat transported by conduction (and radiation) and bulk flow motions. If the bulk flow motion is generated by external means, such as a fan, blower, or pump, then the heat transfer process is a forced convection. However, natural convection refers to heat transfer driven by any body forces within the system, including those generated by density gradients (Naterer, 2018).

In 1701, Newton formulated the basis of the convective heat flux definition from a solid surface to a fluid (Sundén, 2012),

$$q_n'' = h(T_w - T_b),\tag{2.1}$$

where h is called convective heat transfer coefficient, T_w is the wall temperature, and T_b is the bulk temperature. Equation 2.1 is commonly referred to as Newton's law of cooling. The convective heat transfer coefficient (h) is indeed an intricate function of thermophysical properties (density, viscosity, specific heat, thermal conductivity), flow conditions, geometrical features of surface involved in the heat transfer process. The fluid bulk temperature over the pipe cross-section is mathematically defined as,

$$T_b = \frac{1}{\dot{m}c_p} \int_{A_c} \rho u c_p T \, dA_c.\tag{2.2}$$

Here, T and u represent fluid temperature and velocity fields, respectively. Cross-sectional area of the pipe is denoted by A_c and $\dot{m}$ is mass flow rate. Density and specific heat properties of working fluid are symbolized by ρ and c_p, respectively. The bulk temperature is a very essential property for confined flows (e.g., pipe and channel flows). When multiplied with the mass flow rate and specific heat, this quantity represents the rate at which thermal energy is advected with the flow in the pipe. Introducing the bulk temperature, fully-developed thermal conditions are formally defined by Bergman et al. (2011) as,

$$\frac{\partial}{\partial x}\left[\frac{T_w(x) - T(r,x)}{T_w(x) - T_b(x)}\right] = 0. \tag{2.3}$$

The impacts of targeted wall shape in pipes on convective heat transfer are characterized by quantifying variations in local Nusselt number compared to a smooth (regular) pipe. Local Nusselt number (Nu) is a dimensionless number, defined as the ratio of convection to conduction heat transfer. It provides a measure of convective heat transfer close to the wall. The formulation of local Nusselt number is:

$$Nu = \frac{hc}{k_f}, \tag{2.4}$$

in which c represents the characteristic length and k_f is thermal conductivity of fluid.

The local Nusselt number in a turbulent smooth-pipe flow can be evaluated based on existing empirical correlations, such as Petukhov correlation (Petukhov, 1970):

$$Nu = \frac{(f/8)\, Re\, Pr}{1.07 + 12.7(f/8)^{1/2}\,(Pr^{2/3} - 1)}, \tag{2.5}$$

where f is friction factor and Pr is Prandtl number.

11

2.2 Fundamentals of Fluid Dynamics

Batchelor (2000) describes a simple fluid as a material that can deform continuously under the influence of an applied sensible shear force. Fluid dynamics is the study of motions, energy, and forces exerted on or caused by a fluid substance. In a continuum fluid medium, stress (σ) is defined as the internal forces that adjacent molecules apply on each other per unit area, which is mathematically formulated as,

$$\sigma_{ij} = \frac{F_i}{A_j} \tag{2.6}$$

where σ_{ij}, F_i, and A_j symbolize the stress tensor, exerted force, and the planar area on which forces are performed, respectively.

The precise description of a fluid state has been illustrated and assorted based on the fluid viscosity, compressibility, steadiness, and randomness. As stated by Batchelor (2000), dynamic viscosity (μ) is a fluid property that can be mathematically defined as the tangential stress divided by the flow velocity gradient:

$$\mu = \frac{\sigma_{ij}}{\nabla_i u_j} \tag{2.7}$$

The fluid viscosity is very critical in flow dynamics, since it characterizes the fluid response to deformations. A viscous flow experiences the effects of internal frictional forces due to the presence of velocity gradients between adjacent fluid layers (Batchelor, 2000). According to White and Majdalani (2006), Reynolds number (Re) is a fundamental non-dimensional number that quantifies the ratio of inertial to viscous effects. Re represents a controlling norm of flow state, which indicates the predominate flow features. Reynolds number is expressed as,

$$Re = \frac{\rho u c}{\mu} = \frac{u c}{\nu} \tag{2.8}$$

Here, u denotes the velocity scale, c represents the characteristic length scale, ρ is the fluid density, ν is the fluid kinematic viscosity.

Another fundamental fluid parameter that determines the state of flow is the fluid density (ρ). A compressible flow includes the movement of a fluid with varying density, while incompressible flow is characterized by fluid that has a constant density. All fluids exhibit some level of compressibility, while certain fluids, such as water, are deemed incompressible under atmospheric conditions. As illustrated by John and Anderson (2003), the incompressibility presumption can be applied for flows with Mach numbers below 0.3. Furthermore, flows are classified as steady or unsteady. In steady flows, flow features are time-independent, and the spatial changes dominate (Kuethe, 1976). Contrarily, flow properties of unsteady flows exhibit strong time dependency.

Turbulence is an intricate flow mechanism that emerges at high Reynolds numbers, as a result of propagation of perturbations and energy cascade pertinent to flow structures. Although it is difficult to establish a standard definition of turbulence, the community has characterized turbulent flows based on distinct flow features (Davidson et al., 2018):

Irregularity: The nature of turbulence is irregular and chaotic, though turbulence is statistically deterministic and fully governed by the Navier-Stokes equations.

Diffusivity: Turbulence increases momentum exchange among flow layers, which consequently enhances heat transfer and amplifies frictional drag in internal flows.

Large Reynolds numbers: Turbulent flows occur at high Reynolds numbers. Transition to turbulent behaviour evolves with increasing Reynolds numbers, which is associated with the propagation instabilities. For example, transition to turbulence in pipe flows appears at $Re = 2.3 \times 10^3$.

Three-dimensional: Turbulent flows are unsteady and exhibit three-dimensional characteristics.

Dissipation: Turbulence is dissipative in nature, implying that turbulence kinetic energy that is inherited in the smallest-scale eddies is transformed (dissipated) into heat due to frictional effects. The transport of turbulence kinetic energy from the largest to smallest scales follows a cascade process.

Continuum: Turbulent flows are deemed continuum since the smallest scales of a turbulent flow is still substantially larger than the fluid molecular scale. Therefore, turbulence is a flow characteristic.

2.3 Forced Convection in Turbulent Flow

Most heat transfer processes in engineering applications involve turbulent flows. Turbulent flows at high Reynolds numbers are characterized by an extensive range of time and length scales. This procures to apparently insurmountable challenges in solving Navier-Stokes and energy equations for turbulent flows (Jaluria and Torrance, 2017). Thus, statistical nature of turbulence is essential in analysing convective heat transfer in turbulent flows, such that any flow and thermal property (φ) can be fully described based on its mean ($\overline{\varphi}$) and fluctuating (φ') components utilizing Reynolds decomposition (George, 2013):

$$\varphi(x_i,t) = \overline{\varphi}(x_i,t) + \varphi'(x_i,t). \tag{2.9}$$

Reynolds-Averaged Navier-Stokes (RANS) turbulence models solely target calculation of the mean term, which is mathematically defined as:

$$\overline{\varphi}(x) = \lim_{T_p \to \infty} \frac{1}{T_p} \sum_{i=1}^{T_p} \varphi_i(x,t), \tag{2.10}$$

here, T_p denotes the averaging period.

Following the incorporation of Reynolds decomposition and averaging the Continuity, momentum, and energy equations over time, the final forms of the governing equations are formulated as (Kakac et al., 1995):

$$\frac{\partial \overline{U_i}}{\partial x_i} = 0, \tag{2.11}$$

$$\rho \left(\overline{U_j} \frac{\partial \overline{U_i}}{\partial x_j} \right) = \frac{\partial}{\partial x_j} \left[-\overline{p}\delta_{ij} + \mu \left(\frac{\partial \overline{U_i}}{\partial x_j} + \frac{\partial \overline{U_j}}{\partial x_i} \right) - \rho \overline{u'_i u'_j} \right], \tag{2.12}$$

$$\rho c_p \left(\overline{U_i} \frac{\partial \overline{T}}{\partial x_i} \right) = \frac{\partial}{\partial x_i} \left(\alpha \frac{\partial \overline{T}}{\partial x_i} - \overline{u'_i T'} \right). \tag{2.13}$$

The averaged energy equation (e.g., Eq. 2.13) describes the heat transfer processes in turbulent flows, governed by two distinct mechanisms: molecular (conduction) and turbulent (convection). The averaging of momentum (Eq. 2.12) and energy (Eq. 2.13) equations form additional terms, presented as Reynolds stress tensor $(-\overline{u'_i u'_j})$ and turbulent heat flux $(-\overline{u'_i T'})$. These additional terms denote the transport of momentum and heat due to turbulent convection. Evolution of these terms form the basis of the "closure problem" in turbulence, where the number of governing equations is less than the number of unknown variables. In order to "close" the governing equations, Reynolds stress tensor and turbulent heat flux are modeled based on Boussinesq and Eddy viscosity hypotheses. This suggests a linear dependency of Reynolds stress tensor and turbulent heat flux to the velocity and temperature gradients, respectively:

$$-\overline{u'_i u'_j} = 2\nu_t S_{ij} - \frac{2}{3}\delta_{ij}k, \tag{2.14}$$

$$-\overline{u_i' T'} = \frac{\nu_t}{Pr_t} \frac{\partial \overline{T}}{\partial x_i}, \tag{2.15}$$

where k represents turbulence kinetic energy, δ_{ij} is the Kronecker delta, and S_{ij} denotes the rate of strain tensor. Turbulent Prandtl number (Pr_t) is 0.85, according to the literature (Khaboshan and Nazif, 2018; Churchill, 2002). The local rate of turbulence is characterized knowing the isotropic eddy viscosity (ν_t). The process of modeling eddy viscosity varies among turbulence models, which gives rise to distinct characteristics for one compared to the other, e.g., enhanced near-wall treatment.

2.4   Turbulence Modeling

Accurate numerical modeling of turbulent flow and heat transfer requires an extensive amount of computational power (more cost). This is particularly the case when the geometry involves a complex topology or the working medium flows at a high Reynolds number. RANS turbulence models were formulated to minimize the computational costs, while generating sufficiently-accurate estimations of the mean flow and heat transfer fields. Simulations in Chapters 4 and 5 employs RANS-based $k-\omega$ shear stress transport (SST) formulation for modeling turbulence. The $k-\omega$ (SST) model was incorporated in this study based on its performance in properly predicting main flow and heat transfer features. A comprehensive validation study is presented in Chapter 3. The transport formulations and initial conditions of two-equation turbulence models, including Standard $k-\varepsilon$, Realizable $k-\varepsilon$, $k-\omega$, and SST $k-\omega$, are provided below (OpenCFD, 2019).

2.4.1   Standard $k-\varepsilon$ Model

Standard $k-\varepsilon$ model incorporates the conservation formulations for turbulence kinetic energy (k) and turbulence dissipation rate (ε) such as (Cappelli and Mansour, 2013):

$$\frac{\partial}{\partial x_i}(k\overline{U_i}) = \frac{\partial}{\partial x_i}\left[(v+\frac{v_t}{\sigma_k})\frac{\partial k}{\partial x_i}\right] + P_k - \varepsilon, \tag{2.16}$$

$$\frac{\partial}{\partial x_i}(\varepsilon\overline{U_i}) = \frac{\partial}{\partial x_i}\left[(v+\frac{v_t}{\sigma_\varepsilon})\frac{\partial \varepsilon}{\partial x_i}\right] + \frac{C_1\varepsilon}{k}\left(P_k+C_3\frac{2}{3}k\frac{\partial U_i}{\partial x_i}\right) - C_2\frac{\varepsilon^2}{k}. \tag{2.17}$$

where P_k denotes turbulence kinetic energy production, resulting from the interaction of Reynolds stresses and mean velocity gradients. The eddy viscosity (v_t) is determined by $v_t = C_\mu\frac{k^2}{\varepsilon}$. The model closure coefficients are defined as (Cappelli and Mansour, 2013):

$$C_\mu = 0.09; \ \ C_1 = 1.44; \ \ C_2 = 1.92; \ \ C_3 = 0.0; \ \ \sigma_k = 1.0; \ \ \sigma_\varepsilon = 1.3. \tag{2.18}$$

2.4.2 Realizable $k-\varepsilon$ Model

In realizable $k-\varepsilon$ model, the transport equation of k remains identical to Eq. 2.16, while the ε-equation is defined as (Joshi and Nayak, 2019):

$$\frac{\partial}{\partial x_i}(\varepsilon\overline{U_i}) = \frac{\partial}{\partial x_i}\left[(v+\frac{v_t}{\sigma_\varepsilon})\frac{\partial \varepsilon}{\partial x_i}\right] + C_1|S|\varepsilon - C_2\frac{\varepsilon^2}{k+(v\varepsilon)^{0.5}}. \tag{2.19}$$

Here, the model coefficient (C_μ) is computed by:

$$C_\mu = \frac{1}{A_0+A_s\frac{kU_\infty}{\varepsilon}}, \tag{2.20}$$

where $A_0 = 4.04$ and A_s is a function of the mean velocity gradients. The other model coefficients are provided as (Joshi and Nayak, 2019):

17

$$C_1 = 1.44; \quad C_2 = 1.90; \quad \sigma_k = 1.0; \quad \sigma_\varepsilon = 1.2. \tag{2.21}$$

2.4.3 Standard $k - \omega$ Model

The Standard $k - \omega$ model utilizes the conservation equations of k and ω (specific dissipation rate) to estimate the eddy viscosity. This model was initially employed by Kolmogorov (1941), and then upgraded by Saffman (1970) and Saffman and Wilcox (1974), who showed its adequacy for several turbulent flow simulations. The transport equations of the standards $k - \omega$ model are defined as (Joshi and Nayak, 2019):

$$\frac{\partial}{\partial x_i}(k\overline{U_i}) = \frac{\partial}{\partial x_i}\left[(v + \frac{v_t}{\sigma_k})\frac{\partial k}{\partial x_i}\right] + P_k - \beta^* k\omega, \tag{2.22}$$

$$\frac{\partial}{\partial x_i}(\omega\overline{U_i}) = \frac{\partial}{\partial x_i}\left[\left(v + \frac{v_t}{\sigma_\omega}\right)\frac{\partial \omega}{\partial x_i}\right] + \frac{\gamma}{v_t}P_k - \beta\omega^2 + \frac{\sigma_d}{\omega}\frac{\partial k}{\partial x_i}\frac{\partial \omega}{\partial x_i}. \tag{2.23}$$

Here, $v_t = k/\omega$ and the model coefficients are (Joshi and Nayak, 2019):

$$\beta^* = 0.09; \quad \gamma = 0.52; \quad \sigma_k = 2.0; \quad \sigma_\omega = 2.0. \tag{2.24}$$

2.4.4 Shear Stress Transport $k - \omega$ Model

Shear Stress Transport $k - \omega$ model was proposed by Menter (1993) as a hybrid model combining favourable features of $k - \omega$ and $k - \varepsilon$ models. Particularly, $k - \omega$ model is utilized in the near-wall region, while $k - \varepsilon$ model is employed far from the walls. The activation of $k - \omega$ close to the wall and $k - \varepsilon$ at the core region is controlled for smooth transition by an intricate blending function (F_1), which depends on flow conditions, thermophysical properties, and wall-normal distance. The

18

transport equations of SST $k-\omega$ are formulated as (Menter and Esch, 2001; Joshi and Nayak, 2019):

$$\frac{\partial}{\partial x_i}(k\overline{U_i}) = \frac{\partial}{\partial x_i}\left[(v+\frac{v_t}{\sigma_k})\frac{\partial k}{\partial x_i}\right] + P_k - \beta^* k\omega, \tag{2.25}$$

$$\frac{\partial}{\partial x_i}(\omega\overline{U_i}) = \frac{\partial}{\partial x_i}\left[\left(v+\frac{v_t}{\sigma_\omega}\right)\frac{\partial \omega}{\partial x_i}\right] + \frac{\gamma}{v_t}P_k - \beta\omega^2 + 2(1-F_1)\sigma_{\omega 2}\frac{1}{\omega}\frac{\partial k}{\partial x_i}\frac{\partial \omega}{\partial x_i}. \tag{2.26}$$

Here, closure model coefficients are functions of the blending relation such that, $\phi = F_1\phi_1 + (1-F_1)\phi_2$, where ϕ_1 and ϕ represent coefficients of the $k-\omega$ and $k-\varepsilon$ models, respectively:

$$\sigma_{k1} = 1.176; \quad \sigma_{k2} = 1.0; \quad \sigma_{\omega 1} = 2.0; \quad \sigma_{\omega 2} = 1.168; \quad \gamma_1 = 0.5532;$$
$$\gamma_2 = 0.4403; \quad \beta_1 = 0.075; \quad \beta_2 = 0.0828; \quad \beta^* = 0.09. \tag{2.27}$$

2.4.5 Selection of Turbulence Model

Adequate heat transfer predictions in turbulent flows are mainly contingent on the proper selection of turbulence model. Particularly for heat transfer simulations, the accuracy of numerical predictions is highly impacted by turbulence-scale equation and near-wall treatment. According to Menter and Esch (2001), turbulence models based on ε-equation are not capable of generating accurate results in near-wall region. It is commonly known that these models result in overestimations of the turbulence length scale in flows with high pressure gradients, leading to overpredictions of wall shear stresses and heat transfer rates (Rodi and Scheuerer, 1986). Contrarily, $k-\omega$ turbulence model performs well close to the wall with the capacity to accurately estimate the turbulence length scale, resulting in improved calculations of wall shear stresses and heat transfer coefficients (Wilcox, 1993). A major limitation of the Standard $k-\omega$ model is the strong sensitiv-

19

ity of numerical results to free stream conditions (Menter, 1992). The SST $k - \omega$ model is proposed to effectively exploit the superior performance of $k - \omega$ formulation in the near-wall region without the potential errors related to its sensitivity to free stream conditions (Menter, 1993). It is known that SST $k - \omega$ model is the preferred choice for heat transfer simulations, where near-wall and core regions are modeled with comparable accuracies (Chaube et al., 2006).

On hydrodynamics, we completed a comparison between the Standard $k - \varepsilon$ and SST $k - \omega$ models in predicting a fully-developed mean velocity distribution in a smooth pipe at high Reynolds number (see Figure 2.1). Figure 2.1 demonstrated the adequacy of SST $k - \omega$ formulations in accurately simulating the velocity profile in both near-wall and outer regions, and the largest deviation was within 4% from the experimental data of Hultmark et al. (2013). Contrarily, the Standard $k - \varepsilon$ model showed significant deviations to the experimental results, especially in the near-wall region. The maximum deviation of the Standard $k - \varepsilon$ results was within 14% compared to the experiment. Goswami and Hemmati (2020) examined the performance of four conventional RANS models, including the Standard $k - \varepsilon$, Realizable $k - \varepsilon$, Standard $k - \omega$, and SST $k - \omega$, in simulating turbulent pipe flow past square bar roughness. They confirmed that the results of SST $k - \omega$ model showed a close agreement with the experimental data in the near-wall region, while
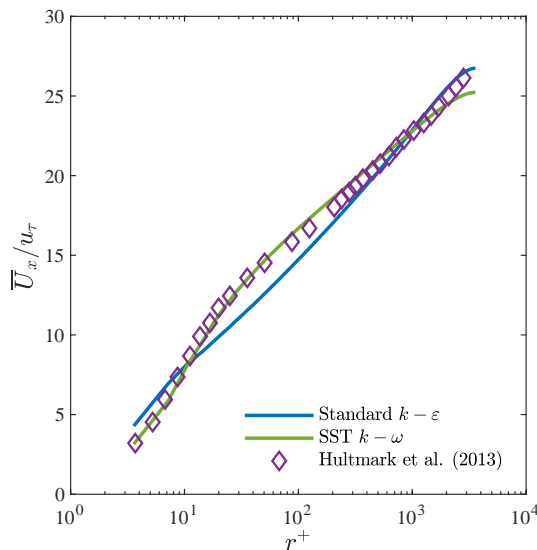
Figure 2.1: Fully-developed velocity profile in a smooth pipe at high Reynolds number.

ε-based models exhibited large deviations. Adequate velocity estimations close to the wall are particularly significant for accurate calculations of wall shear stresses (thereby skin-friction drag coefficients) and heat transfer rates.

On heat transfer, we compared the predictions of fully-developed Nusselt number in a smooth pipe obtained from the Standard $k - \varepsilon$ and SST $k - \omega$ models with Petukhov correlation in Table 2.1. The SST $k - \omega$ formulations predicted Nusselt number within 7.6% compared to Petukhov correlation, while the Standard $k - \varepsilon$ model returned substantial deviation. The SST $k - \omega$ turbulence model was validated and utilized in several previous studies (Zheng et al., 2016, 2017; Chaube et al., 2006; Eiamsa-ard and Changcharoen, 2011), which confirmed the model adequacy in predicting convective heat transfer features in turbulent flows disturbed by geometric wall modifications. Particularly, Zheng et al. (2016, 2017) tested the predictions of RANS-based turbulence models (Standard $k - \varepsilon$, Realizable $k - \varepsilon$, and SST $k - \omega$) to heat transfer characteristics in an internally-grooved pipe. They demonstrated that the SST $k - \omega$ predictions provided the closet numerical results to experimental data and the maximum deviation was 6%. Further, Chaube et al. (2006) and Eiamsa-ard and Changcharoen (2011) confirmed that the SST $k - \omega$ was adequate in estimating heat transfer rates of turbulent flows past square roughness elements. The discussions and observations thus far motivated us to validate and employ the SST $k - \omega$ formulations for modeling turbulence in the current study. A thorough validation study is provided in Chapter 3.

Table 2.1: Comparing Nusselt numbers with Petukhov correlation.

Parameter	Nu	Deviation
Standard $k - \varepsilon$	1214.7	48.0%
SST $k - \omega$	758.3	7.6%
Petukhov correlation	820.8	

2.4.6 Initial Conditions

As indicated by Vold (2017), for isotropic turbulent flows, turbulence kinetic energy field (k) can be initialized using:

$$k = \frac{3}{2}(I \, U_\infty)^2,$$

(2.28)

where I represents the turbulence intensity, and U_∞ is bulk velocity at the inlet boundary (for the pipeflow simulations). Similarly, the turbulence specific dissipation (ω) is initially estimated by:

$$\omega = C_\mu^{-0.25} \frac{k^{0.5}}{l}.$$

(2.29)

Here, $C_\mu = 0.09$ is a model constant, and l is turbulent length scale, defined as $l = 0.038D$, where D refers to hydraulic diameter of the pipe (Greenshields et al., 2015; Pope and Pope, 2000).

2.5 Flow Manipulation Techniques

Limited studies exist in literature regarding the attenuation of convective heat transfer in turbulent flows, despite their practical importance in suppressing heat dissipation in subsurface thermal systems. Contrarily, flow manipulation techniques that aim to enhance convective heat transfer in wall-bounded flows have been the focus of many studies within the thermal sciences and engineering community. Heat transfer intensification methods are broadly categorized into three classes, i.e., active, passive, and compound (Liu and Sakr, 2013). Passive methods employ modifications in surface geometry, which include deployment of wall-mounted perturbations (Menni et al., 2019), change in cross-sectional shape (Zambaux et al., 2015; Tiruselvam et al., 2012), and presence of wall curvature in the form of corrugated and wavy surfaces (Kongkaitpaiboon et al., 2019; Promthaisong et al., 2016). The modifications in wall shape are essentially aimed to promote

effective transverse entrainment between wall and core flow regions and introduce local turbulence (Yang et al., 2020). These flow manipulations lead to effective disturbance of thermal boundary layer, resulting in enhanced heat transfer. However, an increase in pressure drop is the unavoidable drawback of deploying such augmentation technique, causing an increase in pumping power (Alam and Kim, 2018).

In view of its capability in enhancing heat transfer rates with relatively easy installation in an existing thermal system, wall-mounted perturbations have been implemented in staggered or in-line, longitudinal or transverse configurations (Promvonge and Kwankaomeng, 2010). Berner et al. (1984) conducted an experimental study to analyze the main flow features in a duct with segmental baffles. They concluded that the flow attained a fully-recovered state after an axial distance, downstream of the perturbation. Turbulent flow around a surface-mounted rectangular perturbation with varying dimensions was numerically investigated by Hwang et al. (1999). The results revealed the existence of a recirculation region, which was highly influenced by the rib dimensions. Gajusingh et al. (2010) conducted an experimental study to quantify the predominant changes in turbulent flow characteristics due to the introduction of a rectangular baffle in the fully-developed region. Their results demonstrated that the deployment of the insert caused a substantial intensification in turbulence levels. They concluded that an appreciable enhancement in heat transfer rates would be obtained due to the increased turbulence levels associated with the insertion. Habib et al. (1988) computationally analyzed turbulent flow and heat transfer characteristics in a channel with staggered obstructions of various heights and spacings. The results revealed that improvement in heat transfer rates was achieved with increasing the obstacle height and Reynolds number and with decreasing the obstacle spacing. Siddiqui et al. (2007) demonstrated that substantial heat transfer enhancement with a minimum pressure drop was obtained by placing an inclined wall-mounted perturbation inside a pipe. Tandiroglu and Ayhan (2006) examined the hydrodynamic and thermal characteristics of unsteady turbulent pipe flow with baffle insertions. This detailed experimental investigation was conducted using nine inserted tubes at Reynolds numbers of $3,000 \leq Re \leq 20,000$.

The authors proposed two general empirical correlations for time-averaged Nusselt number and time-averaged friction factor, which could serve as tools for an optimization analysis.

Artificial roughness elements have significant impacts on local and overall convective heat transfer coefficients. In the study of turbulent flow past transverse ribs attached on a duct surface, Nusselt number was doubled in comparison to smooth wall condition, while an increment of 4.25 was obtained for friction factor ratio (Prasad and Saini, 1988). Lu and Jiang (2006) sketched the effects of inclined roughness elements on the heat transfer and friction factor characteristics. The orientation of the roughness element with respect to the flow direction was varied between $0°$ to $90°$. At angles of $20°$ and $60°$, the overall thermo-hydraulic performance was superior. Promvonge and Thianpong (2008) studied the effects of ribs in various shapes (rectangular, triangular, and wedge) installed in different arrangements (staggered or in-line) on flow and heat transfer characteristics of fully-developed turbulent flow at $Re = 4 \times 10^3 - 16 \times 10^3$. For similar operating conditions, inline configuration of wedged elements presented higher heat transfer coefficient and friction factor. Further, a three-dimensional numerical study examined heat transfer implications of four different roughness elements with targeted cross-sectional shapes (circular, square, trapezoidal, and saw-tooth) (Singh et al., 2015). The deployment of saw-tooth rib resulted in higher convective heat transfer coefficients.

Modifications to the pipe cross-section have considerable impacts on inducing vortical motions, resulting in better mixing and augmented heat transfer (Meng et al., 2005; Li et al., 2006). Patankar et al. (1977) performed the first numerical investigation on the characteristics of flow and convective heat transfer in ducts with cyclic-axial alterations in cross-sectional shape. The authors generalized the concept of fully-developed flow condition to accommodate these geometrical variations. Guo et al. (1998) suggested that heat transfer process can be intensified by increasing the included angle between temperature gradient and velocity vectors. This ensured that flow entrainment is directed towards the wall boundary, thus increasing radial thermal gradients, which result in higher convective heat transfer coefficients. Following this principle, which is now referred to as field synergy principle, a novel pipe configuration, named as alternating elliptical axis (AEA)

tube, was proposed by Meng (2003). The AEA tube was constructed from elliptical tube segments with varying axes, which were bridged using transition joints. The thermal-hydraulic performance of AEA pipe configuration was investigated experimentally by Meng et al. (2005) and numerically by Li et al. (2006). They concluded that changes in the cross-sectional geometry in AEA tube induced multi-longitudinal vortical flow motions, which contributed to a substantial intensification in convective heat transfer. Khaboshan and Nazif (2018) simulated turbulent forced-convection flow to study the impacts of alternating angle, defined as the angle between the major axis of elliptical cross-sectional planes of the AEA tube, on heat transfer characteristics. The results revealed that increasing the alternating angle led to the increase in the number of longitudinal vortices from four to eight. Inducing more vortical motions in the tube resulted in better entrainment of the core flow towards the near-wall region, which eventually led to augmented heat transfer.

Given the superior performance of wavy surfaces in intensifying convective heat transfer, wavy-walled passages have been commonly implemented in several thermal applications, where geometrical constraints are stringent (Ramgadia and Saha, 2013). Turbulent flow past wavy-walled passage was first investigated by Goldstein Jr and Sparrow (1977). Their results indicated a three-times increase in convective heat transfer coefficient compared to smooth channel flow for low Reynolds number turbulent flows ($Re = 6.0 \times 10^3 - 8.0 \times 10^3$). Later on, it was discovered that wavy-walled passages contributed to a significant enhancement of convective heat transfer only when the flow was in the transitional-flow regime, at which self-sustained oscillatory flow structures were detected (Wang and Vanka, 1995; Ničeno and Nobile, 2001). This was attributed to the self-persisted oscillatory flow motions, which destabilized thermal boundary layer and enhanced entrainment between near-wall and core flow regions. This consequently provided a mechanism for heat transfer enhancement. Large eddy simulations (LES) were conducted by Choi and Suzuki (2005) to study heat transfer characteristics of turbulent flow over a channel with one wavy surface. It was elaborated that the surface modification caused the separation of the turbulent shear layer and the formation of near-wall streamwise vortical structures. The imprints of these flow features on the augmentation of the convective heat transfer coefficient were emphasized. Further, Kruse

et al. (2003) and Kruse and Von Rohr (2006) experimentally studied turbulent heat flux of water channel flow with a wavy heated surface. Through detailed inspections, it was revealed that large scale flow motions had the profound effects on the streamwise component of turbulent heat flux while the wall-normal heat flux was mainly dominated by small scale flow structures. Following that, Kuhn et al. (2010) simulated three-dimensional turbulent flow over a wavy heated wall and studied the imprints of coherent flow structures on the distribution of the connective heat transfer coefficient. The spatial reorganization of coherent flow structures caused a substantial increase in the overall heat transfer coefficient, up to 2.5 compared to the flat channel configuration.

2.6   Reducing Heat Convection and Frictional Drag

Heat transfer enhancement methods have been extensively documented in literature, as was discussed earlier, due to its vital significance for energy conversion processes, chemical processing, and power production (Manglik, 2003; Liu and Sakr, 2013). However, a knowledge gap exists in literature on flow manipulation techniques that aim to reduce near-wall heat convection in turbulent flows. The potential reduction of convective heat transfer in wall-bounded turbulence is of great economic and ecological benefits for extraction processes of energy in geothermal applications (Xu et al., 2015; Phuoc et al., 2019) and energy recovery processes from depleted oil sands reservoirs Wang (2021).

The resemblance between Reynolds-averaged momentum and energy equations naturally procures to the anticipation of similarity between temperature and velocity distributions within the boundary layer. Reynolds (1901) elucidated the presence of correlation between wall shear stress and heat flux through the so-called Reynolds analogy theory. This suggests that flow mechanisms that aim at decreasing skin-friction drag are capable of attenuating convective heat transfer. Therefore, the theory hints at the feasibility of exploiting drag-reducing methods to generate analogous impacts in favor of mitigating convective heat transfer.

Flow control techniques for friction drag reduction in turbulent flows were first emerged in 1970s and continue inspiring many researchers today (Corke and Thomas, 2018). The general strategy to reduce skin-friction drag arises from the cumulative knowledge on turbulent boundary layers as being consisted of unsteady and dynamically-interactive coherent structures. The formation of organised structures in enclosed turbulence plays a central role in flow dynamics (Robinson, 1991). According to flow visualizations of turbulent boundary layers, these near-wall coherent structures are accountable for generating low- and high- speed streaks, through which low-momentum fluid near the wall is replaced by high-moving fluid by vortex updraft and downdraft mechanisms (Waleffe, 1997). Consequently, wall shear stresses reach their maximum magnitudes since high-momentum fluid is pulled towards the wall boundary (Lumley and Blossey, 1998). Further, these energetic coherent structures are viewed to intermittently burst, accounting for more than 80% of turbulence production, and they are believed to increase skin-friction drag and convective heat transfer coefficients (Corke and Thomas, 2018; Lumley and Blossey, 1998; Hamilton et al., 1995). Therefore, successful deployments of flow control methods to suppress the generation and interaction of coherent structures will attenuate momentum entrainment in near-wall region, leading to reductions in skin-friction and convective heat transfer coefficients (Corke and Thomas, 2018; Lumley and Blossey, 1998).

In general, passive flow control methods are more desirable because they do neither necessitate the use of additional sensors and actuators nor require a continual power supply to operate (Spalart and McLean, 2011). Micro-textured walls are deemed as one of the earliest and highly-reviewed strategies of drag control in enclosed turbulent flows (Bushnell, 1990). Particularly, arrays of streamwise-aligned microgrooves (riblets), inspired by topological features on shark skin, were distended from the wall to reduce skin-friction drag and convective heat transfer (Walsh, 1980, 1982; Stalio and Nobile, 2003). Drag reductions of $\sim$10% were obtained with the use of riblets and were found to be impacted by the height and alignment of riblets (Choi et al., 1993; Bechert et al., 1997). Further, it was recognized that the drag-reducing capability of riblets was degraded with increasing bulk Reynolds number of base flow (Spalart and McLean, 2011; Bechert et al., 1997).

In turbulent flows hampered by riblets, the reduction in skin-friction drag was linked to the riblets impeding cross-flow turbulent fluctuations close to the wall and lifting the streamwise vortical structures off the wall, thus providing flow mechanisms to reduce wall shear stress and skin-friction drag (Choi et al., 1993; Bechert et al., 1997; Garcia-Mayoral and Jiménez, 2011). Despite the prospect of riblets to inhibit heat losses in thermal applications, limited investigations are available in literature that deal with changes in convective heat transfer properties over riblet walls. Based on the Reynolds analogy, as the presence of riblets causes damping to turbulent motions in the near-wall region, it is anticipated that the use of riblets would mitigate convective heat transfer. Stalio and Nobile (2003) conducted direct numerical simulations at friction Reynolds number of 180 to investigate impacts of riblets on heat transfer. Results revealed reductions in convective heat transfer coefficients for all examined designs and configurations. This was complemented by the analysis of Jin and Herwig (2014), which attributed the decrease in heat transfer to the lift-off flow impact of riblets on near-wall turbulent structures.

Lately, experimental and numerical findings have sparked an interest in superhydrophobic surfaces as a means to reduce skin-friction drag and convective heat transfer in turbulent flows (Daniello et al., 2009; Rothstein, 2010; Lv and Zhang, 2016). Superhydrophobic surfaces are mainly characterized as surfaces with apparent receding contact angle surpassing 150° (Schellenberger et al., 2016), in which a micro- or nano-sized roughness is artificially employed on a non-wetting wall to generate a gas-liquid interface (Cassie–Baxter state) (Rothstein, 2010; Cassie and Baxter, 1944). Air bubbles are pined within the roughness cavities to locally inhibit direct contact between working fluid and the rugged wall, thus leading to generation of an effective slip velocity at the wall in lieu of the ordinary no-slip condition. Significant reductions in skin-friction drag have been documented in wall-bounded turbulence, e.g., channel (Park et al., 2013) and pipe (Costantini et al., 2018) flows, and turbulent boundary layer flows (Park et al., 2014) with the deployment of superhydrophobic surfaces. The formation of wall slip was shown to be the predominant ground for drag reductions with superhydrophobic surfaces since it causes a fraction of the flow rate to stream inviscidly (Rastegari and Akhavan, 2018). Further, inspections of turbulent

structures revealed that superhydrophobic surfaces weaken near-wall vortical motions, resulting in lower skin-friction coefficients (Park et al., 2013; Rastegari and Akhavan, 2018). Implications of superhydrophobic surfaces on convective heat transfer in turbulent pipe flow were experimentally examined by Lv and Zhang (2016). A decrease in convective heat transfer was observed compared to smooth wall condition. The reduction in heat transfer was linked to the suppression of thermal transport by the trapped air within the roughness cavities. Direct numerical simulations of Fuaad and Prakash (2017) depicted an inhibition of temperature fluctuations and heat fluxes in the near-wall region, leading to reduction in convective heat transfer coefficients. The superhydrophobic effect of a wall is only attained if the Cassie–Baxter state is maintained, e.g., the generated gas-liquid interface does not collapse (Rothstein, 2010). It was found that the resulting gas-liquid layer is prone to cave under high shear stresses of turbulent flows (Checco et al., 2014). Further, the generated composite interface was found to collapse more vigorously with increasing Reynolds number (Aljallis et al., 2013). This has inspired extended investigations to complement the robustness and durability of superhydrophobic surfaces (Wang et al., 2007; Lee and Kim, 2009; Cha et al., 2010).

A crucial aspect in engineering design of flow control devices, as emphasized by Spalart and McLean (2011), is their capability to induce long-lasting and favorable impacts on friction drag and convective heat transfer in the downstream wake. This has inspired several studies to focus on turbulent flow response and recovery past sudden surface perturbations. Jiménez (2004) noted that small-sized steps can cause a considerable effect on skin-friction drag and promote prolong flow changes in the downstream region. Smits et al. (2019) presented flow control strategy by investigating the response and recovery of fully-developed turbulent pipe flow hampered by an axisymmetric square bar roughness element at Reynolds number of 1.56×10^5. The bar height was varied such that, $h/D = 0.05$ and 0.1, where D is hydraulic diameter, and measurements were conducted up to an axial distance of $100h$ downstream the perturbation. It was depicted that the flow did not recover to its equilibrium condition at $100h$. This hinted to a long-lasting recovery behaviour, which was attributed to the slow collapse rate of Reynolds shear stress distribution to-

wards the equilibrium state. They further indicated that the Reynolds shear stress translated away from the wall with a power-law mode, thus providing flow mechanism to generate an extended downstream zone of reduced friction drag and convective heat transfer. Goswami and Hemmati (2020) expanded the work of Smits et al. (2019) and performed numerical simulations to assess impacts of the number of roughness elements, their separation pattern, and periodicity on the overall response and recovery. An asymptotic behavior in the flow response and recovery was observed with increasing the number of bars over three elements in a periodic configuration. Further, they presented considerable impacts of Reynolds number on flow characteristics over the roughness elements (Goswami and Hemmati, 2021).

Recently, Van Buren et al. (2017) examined the response of fully-developed turbulent pipe flow at $Re = 1.58 \times 10^5$ to sudden modifications in pipe shape, constructed to tamper large scale motions and very large scale motions. Particularly, the modified wall geometries were designed to target specific azimuthal Fourier modes of $m = 3$, $m = 15$, and $m = 3 + 15$. The experimental results unveiled that the adopted wall perturbations successfully manipulated the targeted near-wall flow motions depending on the desired Fourier mode. Further, it was observed that the targeted wall conditions caused the mean flow to decelerate and turbulence to decay near the wall, immediately downstream of the pipe-insert. Following the experimental work of Van Buren et al. (2017), Masoumifar et al. (2021a) numerically investigated the recovery of mean flow and turbulent properties in the presence of these pipe wall perturbations at identical Reynolds number. The simulations showed that the lower Fourier mode ($m = 3$) caused the flow to behave monotonically in downstream wake, leading to a relatively faster recovery process compared to the other wall shapes. Contrarily, the higher ($m = 15$) and superimposed ($m = 3 + 15$) Fourier mode shapes depicted a non-monotonic (oscillatory) flow response downstream the perturbation, causing a delay in retrieving the fully-developed condition until $45D$ from the insert.

Masoumifar et al. (2021b) highlighted significant Reynolds-number effects on manipulating turbulent flow response and recovery in pipes with abrupt wall changes. Simulations were conducted for Reynolds number range of 5×10^3-1.58×10^5. They observed similar Reynolds-number

impacts on flow recovery for all three wall shapes. The results revealed the existence of two peaks in mean velocity profile along the wake centerline. The magnitude of the second peak decreased with increasing Reynolds number and its location moved downstream away from the pipe insert following a power-law mode. This caused a delayed recovery behaviour of mean velocity and turbulence kinetic energy with increasing bulk Reynolds number, thus leading to an extended recovery region. The results further indicated that the flow recovery reached an asymptotic trend at $Re \geq 7.5 \times 10^4$, where changes in flow recovery length was less than 3% compared to the highest Reynolds number case.

The recent examinations of Van Buren et al. (2017) and Masoumifar et al. (2021a,b) have indicated that inserting geometric modifications based on particular Fourier modes result in significant variations in pipe flow characteristics. These flow variations could lead to concurrent reductions in near-wall heat convection and skin-frictional drag, hence presenting feasibility to suppress heat losses to ground rock formations in subsurface thermal systems with saving pumping power. In the present study, we concentrate on assessing the performance of targeted wall-shape pipe-inserts on reducing convective heat transfer and frictional drag of turbulent pipe flow at a range of Reynolds numbers.

Chapter 3

METHODOLOGY

This dissertation is motivated by industrial needs for a new technology that lowers heat losses in casings of subsurface thermal systems. Particularly, this study aims to facilitate extraction and harvesting of energy using subsurface thermal resources (e.g., naturally-geothermal and/or depleted oil sands reservoirs) through introducing a new casing pipe system. Significant heat dissipation to ground rock formations was reported as a major obstacle during the extraction of heated fluids from subsurface thermal reserves (Xu et al., 2015; Phuoc et al., 2019). Hence, we aim to restrain near-wall heat convection and frictional drag of turbulent pipe flow by implementing a novel flow manipulation strategy. These hydrodynamic and thermal features could enhance the capacity of subsurface thermal systems.

The present study aims at quantitatively evaluating thermal response and recovery of turbulent pipe flow impeded by targeted wall perturbations at a range of Reynolds numbers, through comparisons against fully-developed smooth-pipe conditions. These comparisons provide detailed characterization on impacts of distinct pipe-inserts on suppressing near-wall heat convection. Similarly, implications of targeted wall shapes on skin-frictional drag are investigated. Geometrical shapes of the targeted perturbations were designed to closely follow three azimuthal Fourier modes of $m = 3$ (Case I), $m = 15$ (Case II), and $m = 3 + 15$ (Case III). According to Van Buren et al. (2017) and Masoumifar et al. (2021a,b), these pipe-inserts are capable of tampering turbulent pipeflow

32

characteristics, which could output desirable implications for enhancing subsurface thermal processes. Schematic illustrations of the targeted perturbations are shown in Figures 1.2, 1.3, and 1.4. A detailed description of the geometrical features of the adopted pipe modifications is present in Section 1.2.

This chapter is prepared to provide a description of the methodology employed in the present study. The numerical setup is detailed in Section 3.1. This is followed by a number of verification studies in Section 3.2. Validation of the turbulence model is presented in Section 3.3.

3.1   Computational setup

We numerically solved the steady-state three-dimensional continuity (Eq. 2.11), momentum (Eq. 2.12), and energy (Eq. 2.13) equations using OpenFOAM. The bulk Reynolds number ranged between 2.5×10^4 and 7.5×10^4, based on $Re = U_\infty D/\nu$, where U_∞ is the averaged flow velocity at the inlet boundary of the smooth pipe, D is the pipe diameter, and ν is kinematic viscosity of working fluid. Thermophysical properties of the fluid were assumed constant and independent from temperature variations. Table 1 presents the fluid thermophysical properties based on film temperature (T_f). Radiation and natural convection heat transfer mechanisms, body forces, and viscous dissipation were presumed to have negligible effects and were not taken into consideration in the present study. Turbulent Prandtl number (Pr_t) was set to 0.85, following previous studied in literature of similar perturbed flows (Khaboshan and Nazif, 2018; Churchill, 2002).

Table 3.1: Thermophysical properties of water at film temperature (T_f).

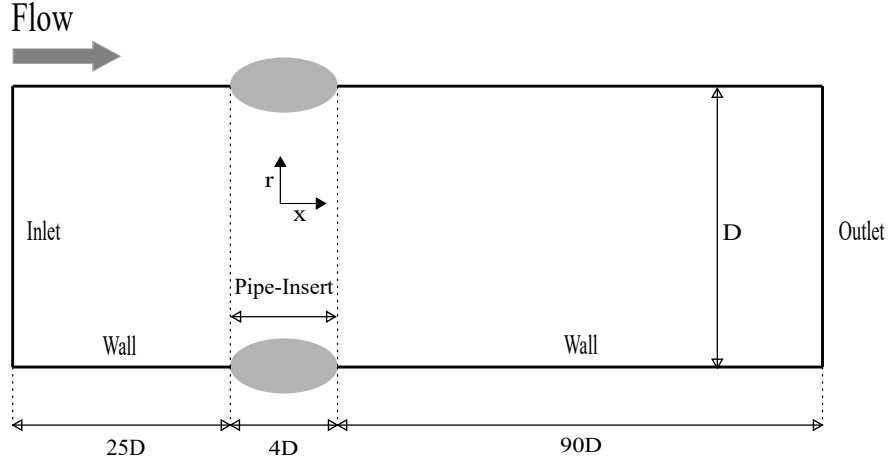| Parameter	Unit	Value
Density (ρ)	kg/m^3	997
Kinematic viscosity (ν)	m^2/s	8.93×10^{-7}
Thermal conductivity (k_f)	W/m.K	0.61
Specific heat capacity (C_p)	J/kg.K	4181

Figure 3.1: Schematic of the computational domain used in the present study (not to scale).

The $k - \omega$ Shear Stress Transport (SST) formulation was utilized to model turbulence in Open-FOAM based on its adequacy in properly capturing main heat transfer characteristics (Menter and Esch, 2001). More details on the performance of RANS-based models is presented in Section 2.4, and a thorough validation study of the employed model is provided in 3.3. OpenFOAM is a well-established finite volume solver (Greenshields et al., 2015), which is broadly used in literature for simulating thermofluid engineering problems (Weihing et al., 2014; Turnow et al., 2011). The governing equations were spatially descritized using second-order accurate schemes. The SIMPLE (Semi-Implicit Method for Pressure-Linked Equations) algorithm was incorporated to couple the pressure and velocity fields.

Schematics of the computational domain is presented in Figure 3.1, which duplicates the experiments of Van Buren et al. Van Buren et al. (2017) and the domain design of Masoumifar et al. Masoumifar et al. (2021b,a). It extends from $-27D$ to $+92D$ in the streamwise ($x-$) direction and involves three main sections: upstream smooth section ($25D$), pipe-insert section ($4D$), and downstream smooth section ($90D$). These upstream and downstream sections were implemented for smooth transition and recovery of the fully-developed turbulent flow, respectively.

A nonuniform structured mesh, including 12.6×10^6 hexahedral elements, was created for all the simulations. Refined mesh elements were placed close to the pipe-insert section to properly capture flow and thermal features in the critical region. A gradual transition to coarser mesh was

34
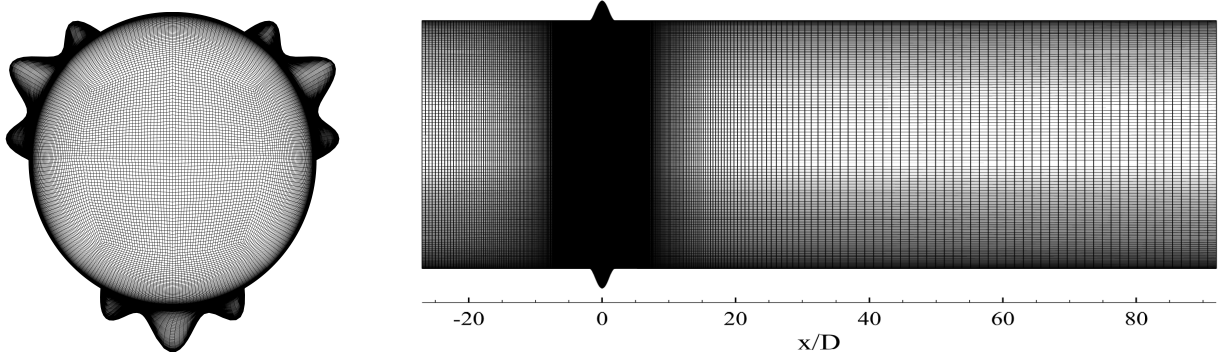
Figure 3.2: Spatial grid distribution over the cross-sectional area and axial plane of the pipe. Case III is presented as an example.

implemented towards the domain boundaries, while the maximum expansion ratio was kept below 1.02. Figure 3.2 depicts the grid distribution along the radial, circumferential, and axial directions. The non-dimensional radial distance of first cell from the wall (r^+) remained below 2.0, as shown in Figure 3.3. The impacts of the domain and grid designs on numerical predictions were examined through a series of sensitivity studies, details of which are provided in the next section.

To obtain fully-developed flow conditions, separate simulations were performed for all Reynolds numbers using a smooth pipe with an axial length of $220D$. The fully developed flow conditions (i.e., Dirichlet and Neumann boundary conditions for velocity and pressure fields, re-
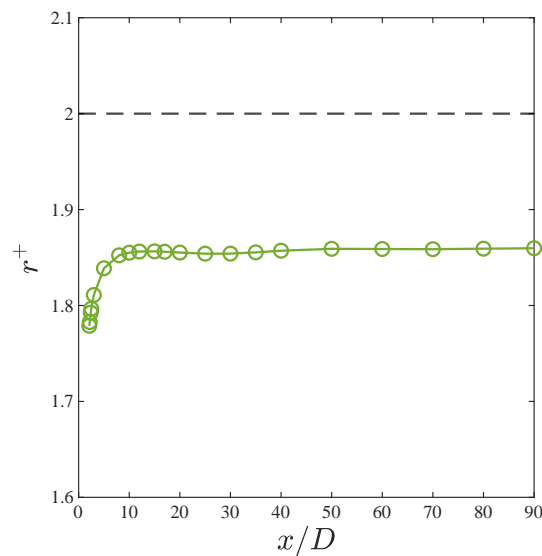
Figure 3.3: Variations of r^+ along the axial direction.

35

spectively) were subsequently mapped and imposed at the inlet boundary of the main simulations at identical Reynolds number. This method was successfully utilized in former investigations of similar perturbed flows (Masoumifar et al., 2021b,a; Goswami and Hemmati, 2021, 2020). A uniform fluid temperature was applied for all simulations at the inlet boundary. A no-slip and isoflux boundary conditions were imposed on the pipe wall. At the outlet boundary, the Neumann boundary condition was employed for all variables, defined as $\partial \phi / \partial n$, where ϕ is any flow and thermal property. All simulations were completed on Compute Canada clusters. The numerical simulations were deemed to be numerically converged when the root-mean-square of momentum and energy residuals dropped below 10^{-6}.

3.2   Verification Studies

The accuracy of numerical solutions is strongly impacted by the computational domain setup and spacial grid quality. We have conducted thorough domain and grid sensitivity studies at $Re = 7.5 \times 10^4$ based on Case III to determine the optimum computational setup, which minimizes all unfavorable effects on numerical predictions. The present results were normalized using the pipe radius and diameter ($D = 2R$), averaged inlet velocity (U_∞), friction velocity (u_τ), and friction temperature (T_τ).

3.2.1   Domain Sensitivity Study

The effects of computational domain on numerical predictions were examined based on three domain sizes, details of which are outlined in Table 3.2. These domains were constructed through successive adjustments of the axial distance of the outlet (downstream) section. The results of domain-sensitivity analysis are presented in Figure 3.4. The axial variations of mean streamwise velocity and turbulence kinetic energy along the wake centerline unveiled that Domain 2 and Domain 3 were sufficiently large to properly capture the recovery of obstructed turbulent flow at $Re = 7.5 \times 10^4$. Further, the maximum difference was less than 2% between simulations using
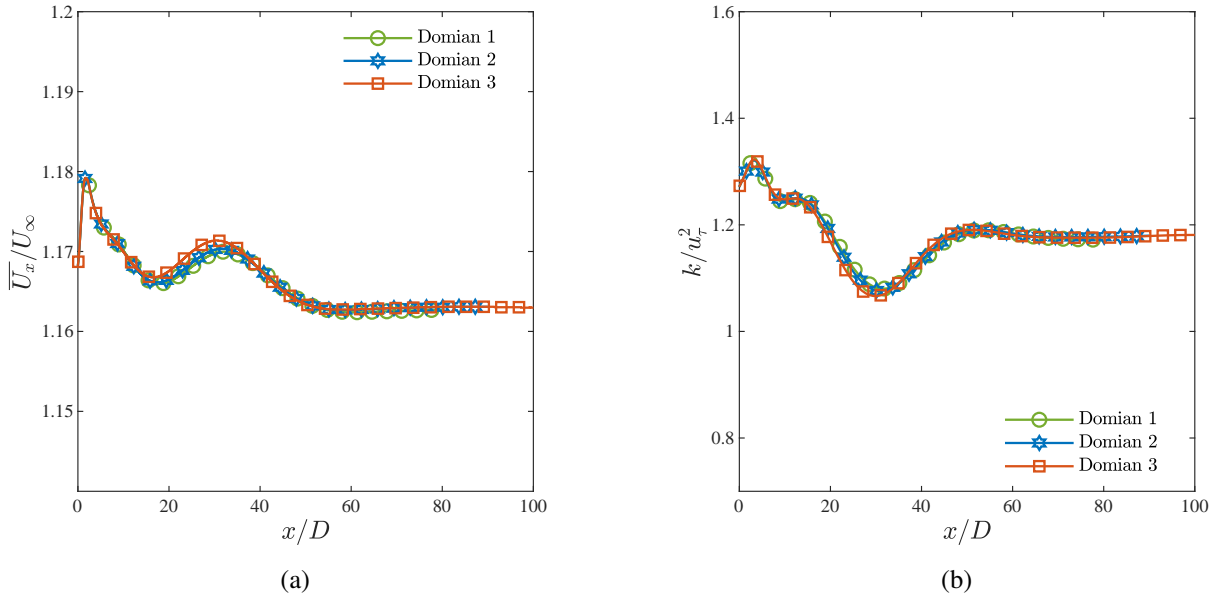
Figure 3.4: Impact of domain size on (a) mean streamwise velocity and (b) turbulence kinetic energy.

Domain 2 and Domain 3. This indicted a minimal impact of the outlet boundary condition on predicting flow variations in the critical region, downstream of the pipe-insert segment. Therefore, Domain 2 with an axial domain extent of $119D$ was employed for the present study.

3.2.2 Grid Sensitivity Study

The impact of spacial grid quality on numerical results was studied using five grid designs, specifics of which are presented in Table 3.2. The grid sensitivity analysis was performed by consecutively increasing the grid resolution in radial, circumferential, and axial directions. The grid sensitivity analysis was completed by studying impacts of the grid on radial distributions of time-averaged streamwise velocity and temperature at different axial locations. For brevity, the radial comparisons of quantities of interest are only presented and discussed at $x/D = 30$. Radial comparisons of mean streamwise velocity and temperature disclosed a small variation of less than 2% between Grid 4 and Grid 5 (see Figure 3.5). This confirmed that Grid 4 (12.6×10^6 hexahedral elements) was sufficient to simulate the main flow and thermal features.
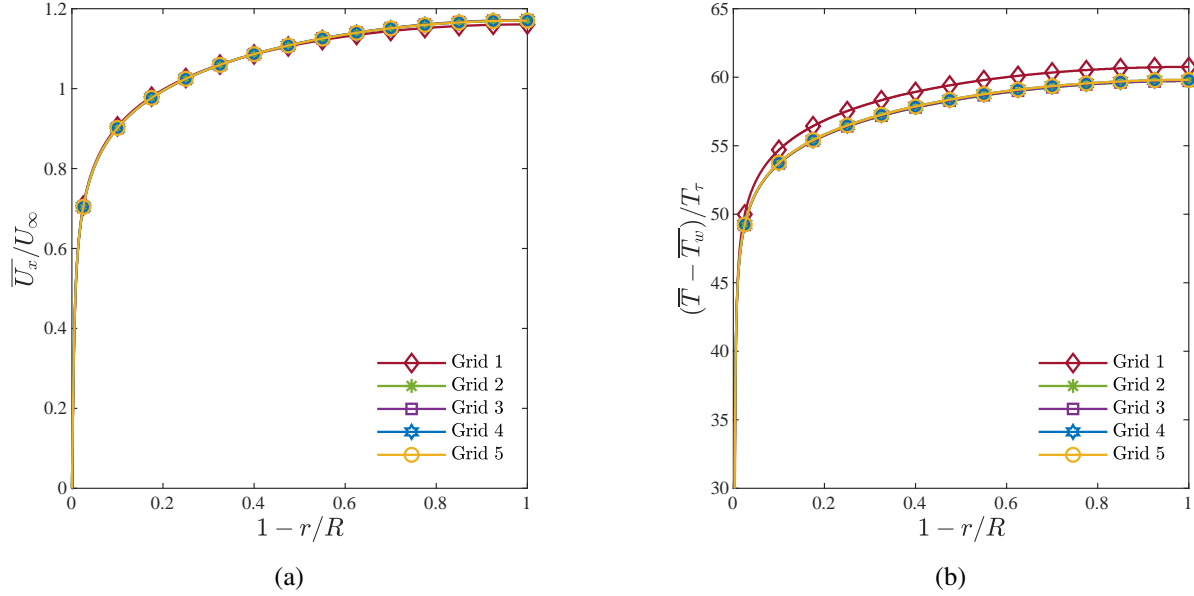
Figure 3.5: Impact of grid refinement on (a) mean streamwise velocity and (b) mean temperature, at $x/D = 30$.

Table 3.2: Grid specifications based on Case III. $\Delta\theta^+$ and Δx^+ are the non-dimensional spacing in the azimuthal and streamwise directions in wall units, respectively. L_{pipe} is the axial pipe length and N_{total} represents the total number of hexahedral elements.

Study	L_{pipe}	N_{total}	r^+	$\Delta\theta^+$	Δx^+
Domain 1	$109D$	12.2×10^6	2	48	49
Domain 2	$119D$	12.6×10^6	2	48	49
Domain 3	$129D$	13.0×10^6	2	48	49
Grid 1	$119D$	8.8×10^6	4	55	49
Grid 2	$119D$	9.3×10^6	2	48	82
Grid 3	$119D$	10.7×10^6	2	48	64
Grid 4	$119D$	12.6×10^6	2	48	49
Grid 5	$119D$	14.2×10^6	2	48	40

3.3 Validation Studies

In an attempt to validate the accuracy of our numerical predictions for main flow and heat transfer properties, we performed simulations on a smooth pipe with an axial length of $220D$ using SST $k - \omega$ turbulence model at $Re = 2.5 \times 10^4 - 7.5 \times 10^4$. The numerically-obtained fully-developed
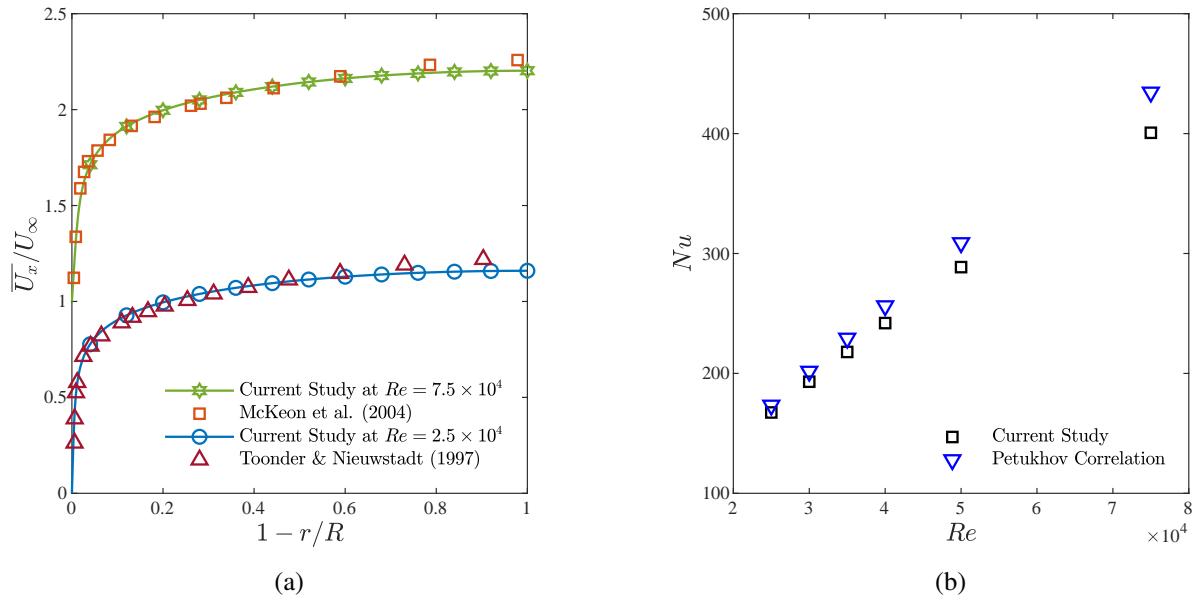
Figure 3.6: Comparing the current numerical results of (a) mean streamwise velocity where the data corresponding to $Re = 2.5 \times 10^4$ was shifted by 1 non-dimensional unit in the vertical direction, and (b) Nusselt number, with experimental data.

velocity profiles were compared with the experiments of Mckeon et al. (2004) at $Re = 7.5 \times 10^4$ and Den Toonder and Nieuwstadt (1997) at $Re = 2.5 \times 10^4$ (see Figure 3.6). The numerical and experimental results agreed well in both near-wall and core flow regions. The maximum differences were within 5% and 4% of the experimental results at the highest and lowest Reynolds numbers, respectively. We further compared the predicted fully-developed Nusselt number for each Reynolds number with Petukhov empirical correlation (Petukhov, 1970). Nusselt number comparisons showed a close agreement with the empirical correlation. The maximum deviation in predicting Nusselt number was within 8% compared to Petukhov correlation (Petukhov, 1970). These quantitative examinations assured that the present numerical model is sufficiently accurate in simulating main hydrodynamic and thermal features of smooth turbulent pipe flows.

3.3.1 Perturbed Flow with Heat Transfer

It is essential to note that there exists no experimental or DNS investigation in literature that provides a detailed description of the mean flow and heat transfer properties in the presence of targeted wall shapes. This has indeed limited our capability to compare the numerical results of the targeted cases ($m = 3$, $m = 15$, and $m = 3 + 15$) with experimental or DNS data. However, we expanded the validation study by simulating turbulent flow with heat transfer hampered by multiple square roughness elements in a wall-bounded domain. This was completed to examine the performance of our numerical model in predicting mean flow and heat transfer characteristics of turbulent flow in the presence of flow perturbations.

Figure 3.7 depicts schematics of the computational domain, which was created to closely replicate the experimental setup of Tanda (2004). Here, the computational domain consists of smooth inlet ($x = 21H$) and outlet ($x = 7H$) sections along with an intermediate ribbed section ($x = 14H$), where H is the channel height. The flow was perturbed inside the ribbed section by periodically placing a total of seven square roughness elements with a height of $e/H = 0.15$ on the lower channel wall. The separation distance (or pitch length d) between consecutive roughness elements was equal to $d/H = 2.0$. A nonuniform spatial grid, with a total of 5.6×10^5 hexahedral elements, was employed for this simulation. The r^+ was set at 4.0, and the maximum expansion ratio was maintained below 1.02. The simulation was conducted in a 2D-symmetric plane at Reynolds number of 2.85×10^4. A uniform velocity profile was applied at the inlet boundary. Neumann boundary condition was set for the pressure field at the inlet boundary and for all variables at the outlet
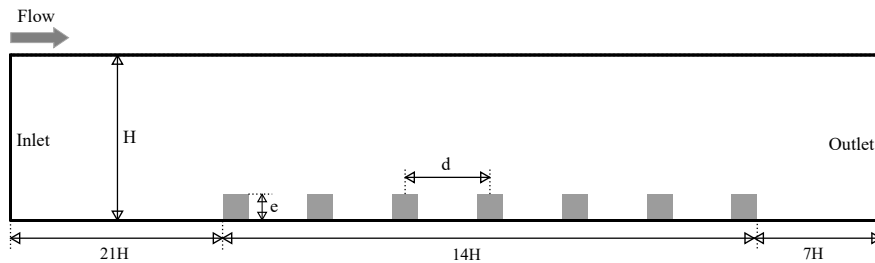
Figure 3.7: Schematics of the computational domain with square roughness elements used for validation (not to scale).

boundary. The pipe wall was subjected to a no-slip boundary condition. Thermally, the flow entered the computational domain with a uniform temperature distribution. A uniform heat flux was imposed on the lower channel wall, while the upper and rib surfaces were considered insulated, following the experiment of Tanda (2004).

Table 3.3: Comparing friction factor (f) of channel flow with square ribs at $Re = 2.85 \times 10^4$.

Study	f	Deviation
Current study	0.0281	6.6%
Tanda (2004)	0.0301	

We compared the numerically-calculated friction factor (f) with the experimental value of Tanda (2004) in Table 3.3, which returned a deviation of 6.6%. The accuracy of our numerical model in predicting heat transfer of perturbed flow was validated by comparing local Nusselt number distribution inside the ribbed section, particularly between the fifth and sixth elements, with experimental data (see Figure 3.8). It was demonstrated that the numerical model provided comparable predictions of Nusselt number to the experimental results of Tanda (2004). The maximum
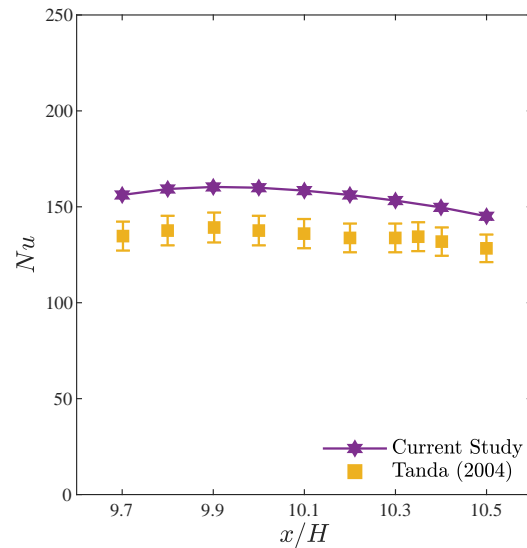
Figure 3.8: Nusselt number distribution of turbulent flow perturbed by square roughness elements. Error bars are presented based on the experiment of Tanda (2004).

deviation was within 16% of the experimental results. These deviations in f and Nu were within the acceptable range, provided that the uncertainty (at 95% confidence level) in the experimental data of friction factor and convective heat transfer coefficient were reported by Tanda (2004) as $\pm 3.4\%$ and $\pm 5.6\%$, respectively. Hence, the thorough validation studies completed here have presented adequate evidence on the accuracy of our numerical model, particularly SST $k - \omega$ turbulence model, in simulating mean flow and heat transfer features. This conclusion was complemented by similar observations in former studies (Chaube et al., 2006; Eiamsa-ard and Changcharoen, 2011; Zheng et al., 2015, 2016, 2017; Tang et al., 2015) with regards to the accuracy of numerical simulations, and specially SST $k - \omega$ turbulence model, in simulating thermofluid characteristics.

Chapter 4

EFFECTS OF PIPE-INSERTS

4.1 Introduction

The thermal response and recovery of turbulent pipe flow past sudden changes in wall shape are numerically investigated at the highest Reynolds number of 7.5×10^4. The adopted wall modifications are designed to follow targeted azimuthal Fourier modes, as previously elaborated in Section 1.2. The results and discussions presented in this chapter characterize the impacts of pipe-wall modifications on reducing convective heat transfer and frictional drag. The outcomes provided here suggest economic and environmental benefits pertinent to subsurface thermal processes, once the final optimum design for the introduced pipe-inserts is determined.

As discussed in Sections 2.5 and 2.6, there exists a knowledge gap in literature regarding the mitigation of convective heat transfer by deploying modifications in wall geometry. Here, we aim to introduce a novel mechanism for transporting heated fluids through subsurface casing that reduces heat losses and frictional drag. This is practically significant to inhibit heat losses associated with the extraction of hot fluids from subsurface resources using one or multiple production wells while saving pumping power, as discussed in Section 1.1. More recently, in response to pipe-wall modifications based on distinct Fourier modes, the experiments of Van Buren et al. (2017) and the simulations of Masoumifar et al. (2021a) presented profound variations in flow features, which

could lead to reductions in heat transfer and friction drag. Particularly, they discovered that these wall-shape modifications, which were constructed to impact large scale motions and very large scale motions in pipe flows, caused a deceleration of mean flow and reduced velocity gradients in near-wall region, downstream of pipe-insert. Masoumifar et al. (2021a) further elaborated a prolong flow recovery zone in response to these wall shapes. These modified flow characteristics could contribute to concurrent reductions in convective heat transfer and frictional drag, hence providing feasibility to minimize heat losses to ground rock formations in subsurface thermal systems with lower pumping power. In this chapter, we build on Van Buren et al. (2017) and Masoumifar et al. (2021a) studies and aim to evaluate effects of targeted pipe-inserts on reducing heat convection and frictional drag at $Re = 7.5 \times 10^4$. The outcomes presented in this chapter could be translated to new fundamental insights, which enable the design and development of new and efficient thermal systems related to geothermal power.

This chapter addresses the first three objectives of this dissertation, as delineated in Section 1.3. This chapter is structured such that a description of the problem is provided in Section 4.2. Illustration of the results and their discussion are presented in Section 4.3. The main conclusions of this chapter are summarized in Section 4.4.

4.2 Problem Description

We numerically investigated impacts of targeted variations in wall shape on convective heat transfer and frictional drag of turbulent pipe flow at Reynolds number of $Re = 7.5 \times 10^4$. The modifications in the pipe wall were implemented by adopting an insertion with an axial length of $4D$, where D is the pipe diameter. Geometries of the inserts were designed to best replicate the setup of Van Buren et al. (2017) and Masoumifar et al. (2021a,b). Graphical representations of targeted pipe-inserts are illustrated in Figures 1.2, 1.3, and 1.4. A detailed description of the targeted pipe inserts is present in Section 1.2.

4.3 Results and Discussion

We begin by examining effects of the adopted wall modifications on radial profiles of mean axial velocity through comparisons against fully-developed state in Figures 4.1(a-c). The fully-developed condition corresponds to the flow and thermal state at $x/D = 90$, downstream of the
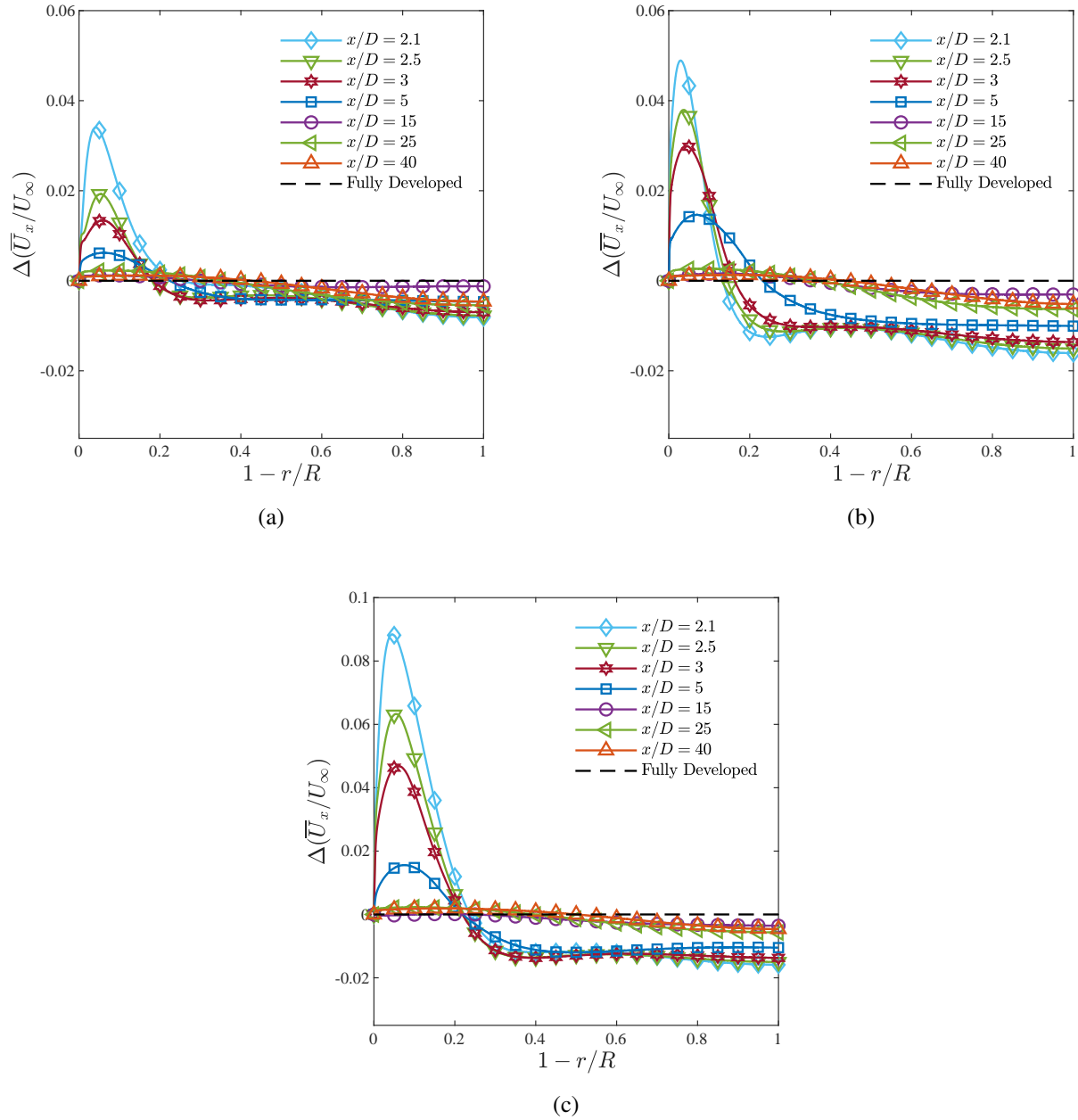

Figure 4.1: Mean streamwise velocity profile development for (a) Case I, (b) Case II, (c) Case III.

insertion section, where no variations in the flow and thermal characteristics were detected in comparison to fully-developed smooth pipe flow at similar operating conditions. The mean streamwise (axial) velocity ($\overline{U_x}$) was normalized using inlet bulk velocity (U_∞) and the radial coordinate (r/R) was normalized by the pipe radius. Variations in streamwise velocity profiles were defined by evaluating local differences (Δ) from fully developed state at $x/D = 90$. Particularly, the radial variations of mean axial velocity were examined at selected axial positions within $2D - 40D$, downstream of the pipe-insert section. Due to the modifications in wall geometry within the pipe-insert segment, the mean axial flow exhibited a velocity-deficit characteristic in near-wall region ($0 < r/R < 0.2$), immediately downstream of the pipe insert, for all three cases. The deficit in velocity fields is presented in Figures 4.1(a-c) as overshoots above the fully-developed state for all three wall shapes. The velocity deficit was balanced by an increase in magnitude of velocity at the outer region. This was consistent with the observations of Van Buren et al. (2017) and Masoumifar et al. (2021b), which elaborated that these wall modifications caused a deceleration and acceleration of mean flow in the near-wall and core flow regions, respectively. The flow adjustments in the core region to balance the velocity deficit in the near-wall region were ascribed to the nature of wall-bounded flows (e.g., channel and pipe flows) (Van Buren et al., 2020). On the thermal and heat flow, the flow deceleration in the near-wall region hinted at a decrease in magnitude of local convective heat transfer in the downstream region. Therefore, the targeted changes in wall shape could cause a drop in local Nusselt number (Nu) distribution after the pipe insert, leading to mitigation of heat losses to surroundings (e.g., ground formations in geothermal applications).

We further examined the axial velocity variations along the wake centerline for all three cases in Figure 4.2. Here, the maximum velocity magnitude from fully-developed profile is used to normalize the axial velocity variations. Figure 4.2 depicts a non-monotonic (oscillatory) flow response for all three cases, such that a peak appears to exist at $x/D = 32$. Past this peak, the flow was noticed to recover towards the fully-developed flow condition for all wall shapes. A similar flow behaviour in the mean velocity profile has been formerly depicted in previous studies of non-equilibrium turbulent flows (Smits et al., 1979). The recovery process of $\overline{U_x}/U_\infty$ was investigated
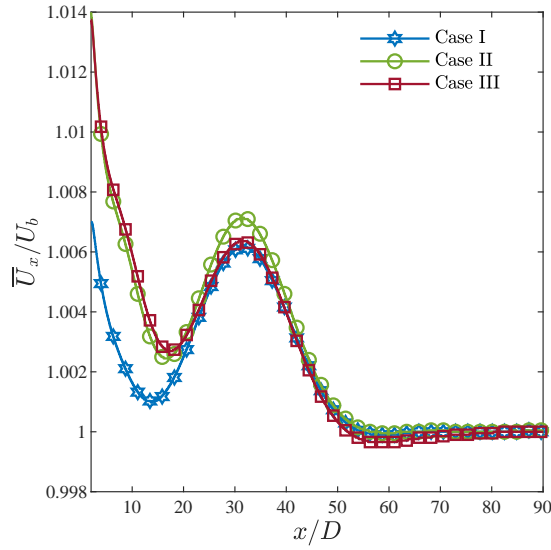
Figure 4.2: Variations of streamwise velocity along the wake centerline for all wall shapes.

for all three cases in the downstream region by depicting the flow relaxation to the fully-developed condition. The recovery behaviour was examined based on maximum variations of less than 0.5% compared to fully-developed condition. We noticed that all three cases showed a delay in retrieving a recovered condition until $x \approx 40D$. This delayed recovery was attributed to the presence of the non-monotonic and oscillating flow response in the downstream region.

The distribution of time-averaged skin friction coefficient along the axial direction is illustrated in Figure 4.3a. The skin friction coefficient was calculated by integrating over the circumferential direction of the pipe wall based on $C_f = \tau_w/0.5\rho U_\infty^2$, where τ_w is the wall shear stress. Skin-friction coefficient (C_f) was normalized by its far downstream value ($C_{f,b}$) at $x/D = 90$, where there exist no variations in flow and thermal characteristics compared to fully-developed smooth-pipe conditions. The axial location was normalized by the pipe diameter D. The distribution of skin friction coefficient exhibited a substantial decrease in magnitude for all cases, compared to the smooth pipe flow at similar operating conditions, before relaxing towards the fully-developed condition. The maximum percentage reductions of C_f were 12.5%, 17.4%, and 16.5% for Case I, Case II, and Case III, respectively (see Figure 4.3b). The decrease in skin friction coefficient was attributed to the flow deceleration and reduced velocity gradients in proximity of the pipe wall. This observation

47
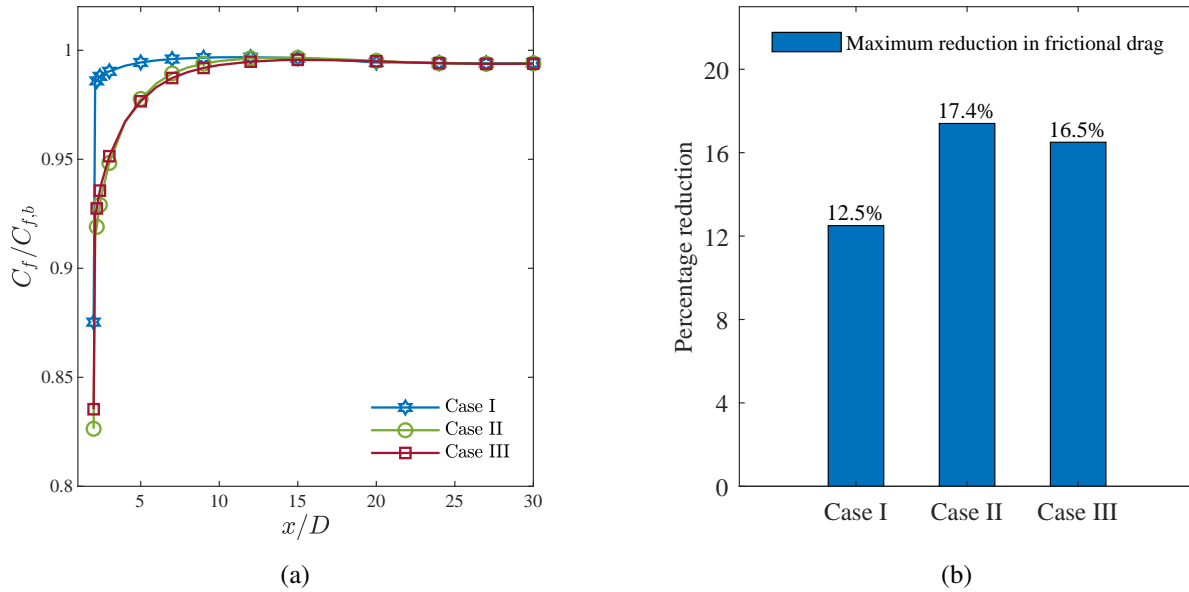
Figure 4.3: Impacts of Fourier pipe-inserts on frictional drag. (a) variations of C_f along the wake axial direction, and (b) maximum frictional-drag reductions for all cases.

agrees well with previous studies, which confirm the capacity of generating reduced-momentum flow close to the wall as a successful flow mechanism to reduce frictional drag (Schoppa and Hussain, 1998; Cheng et al., 2021; Whalley and Choi, 2014; Du et al., 2002; Ramgadia and Saha, 2013). Downstream the pipe-insert within $x = 2D - 10D$, the average reductions in frictional drag were 1.6%, 5.0%, and 4.7% for Case I, Case II, and Case III, respectively. Hence, we can confirm that the targeted wall modifications were capable of generating a downstream zone of reduced drag and lower surface friction. From a practical perspective, these reductions in skin-friction drag may lead to economical and environmental benefits pertinent to several engineering applications (e.g., extraction processes in geothermal systems), once the optimum design for the targeted pipe-inserts is defined based on a series of design optimization studies.

The modified thermal response to the targeted wall shapes is evaluated through inspecting variations in radial profiles of mean temperature with respect to the fully-developed state in Figure 4.4. The mean temperature was normalized by friction temperature, based on $T_\tau = q_w/\rho C_p u_\tau$, where q_w is the uniform heat flux imposed on the pipe wall and u_τ is friction velocity. Immediately
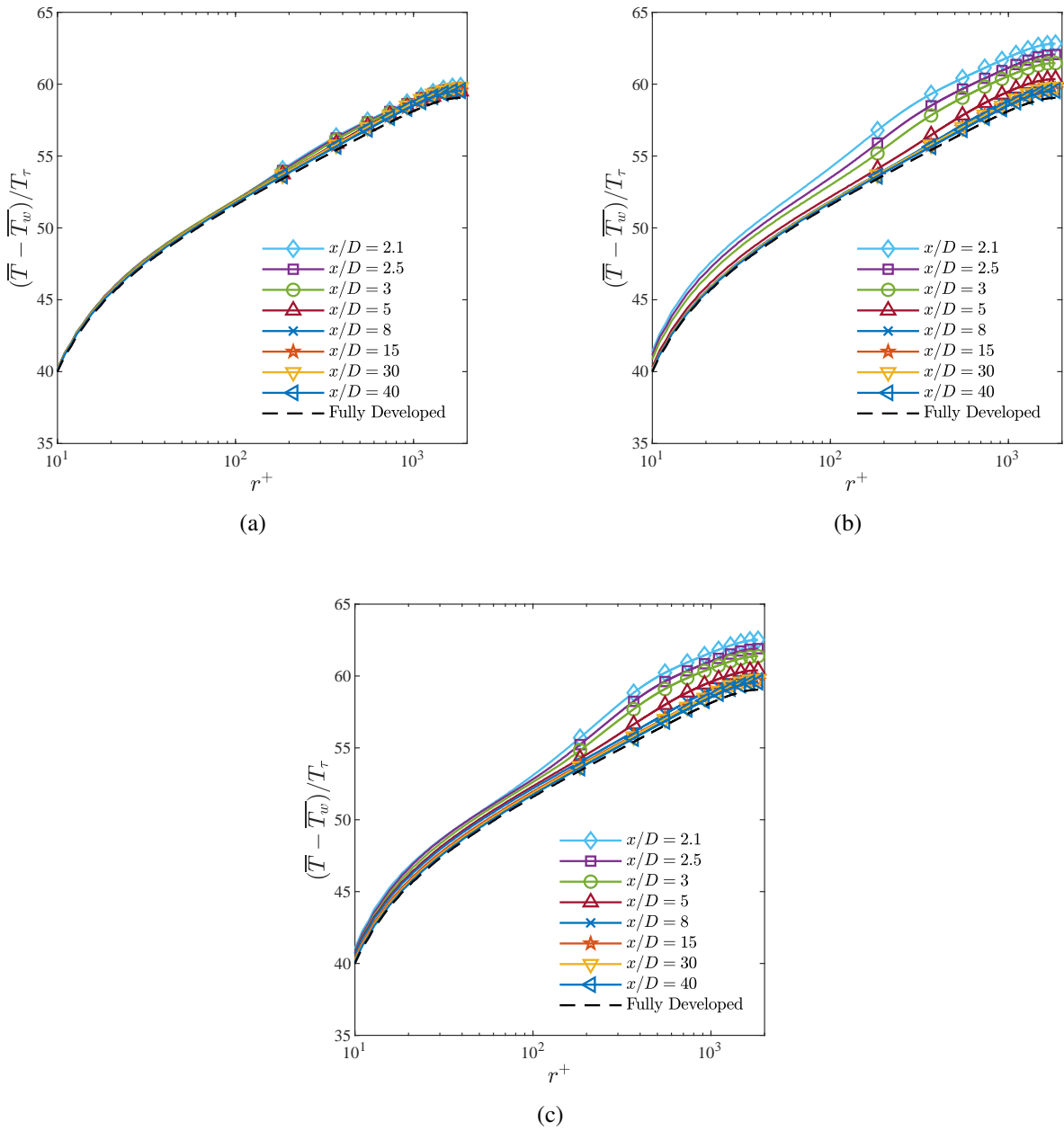
Figure 4.4: Mean temperature profile development for (a) Case I, (b) Case II, (c) Case III.

downstream of the pipe-insert at $x/D = 2.1$, all three cases showed an increase in magnitude of the mean temperature along the radial direction ($r^+ > 10$) compared to the fully-developed state. This was followed by a relaxation of the mean temperature, within $2D - 40D$, towards the fully-recovered condition. The presented results confirmed that the targeted wall perturbations caused

an attenuation in strength of the convective heat transfer mechanism, which resulted in higher fluid temperature, downstream of the pipe insert. This was attributed to the decelerated flows and reduced velocity gradients in the near-wall region, as depicted previously in Figure 4.1. This interpretation was consistent with the discussions of Ramgadia and Saha (2013), while investigating the variations of turbulent heat transfer characteristics in downhill surface of wavy-wall duct. More recently, Castellanos et al. (2022) linked the attenuation in convective heat transfer to the deliberate formation of momentum deficit within the boundary layer. We further looked at the recovery of mean dimensionless temperature by tracing their relaxation behavior towards the fully-developed state within $2D - 40D$, downstream of the pipe perturbation. All three cases depicted a prolong recovery trend, such that the fully-recovered thermal state was attained within $x \approx 40D$. The similarities in the recovery behavior between mean axial velocity and temperature implied that the heat transfer recovery was mainly dominated by velocity gradients downstream of the pipe-insert.

To quantitatively assess the influence of targeted wall shapes on convective heat transfer, the cross-sectional-averaged Nusselt number was computed at several axial locations downstream of
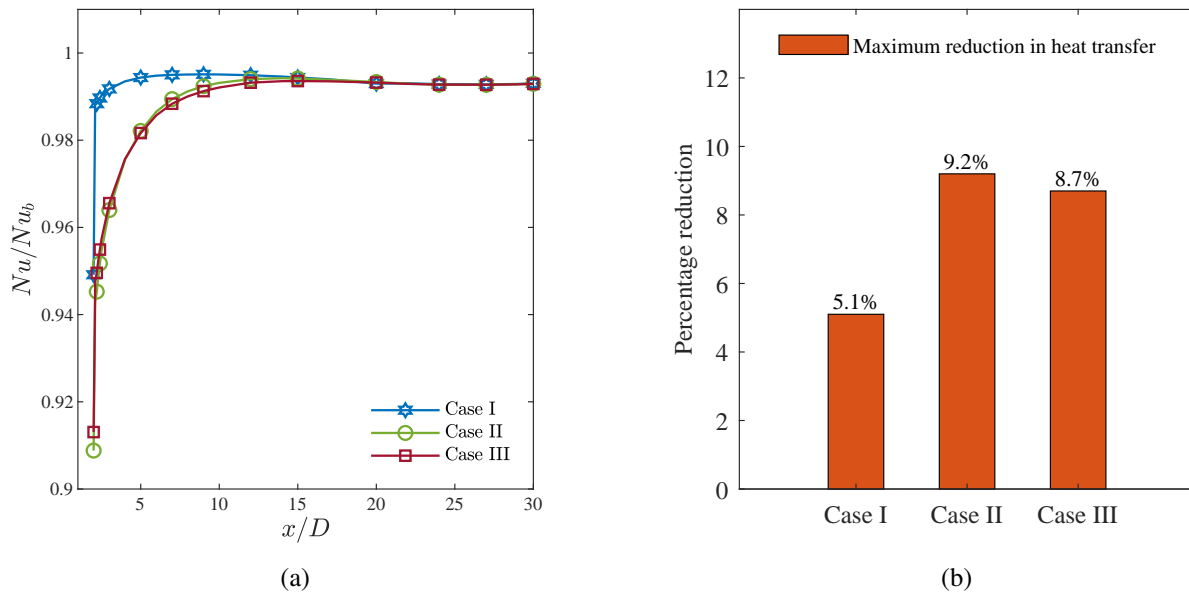

Figure 4.5: Effects of Fourier pipe-inserts on convective heat transfer. (a) variations of *Nu* along the wake axial direction, and (b) maximum heat transfer reductions for all cases.

the pipe insert (Figure 4.5a). Local Nusselt number (Nu) was calculated based on $Nu = hD/k_f$, where h is the convective heat transfer coefficient. Nusselt number (Nu) was normalized by its far downstream value (Nu_b) at $x/D = 90$. The axial variations of local Nusselt number indicated an initial drop in magnitude for all wall shapes, before approaching the fully recovered state. The results demonstrated a maximum reduction of 5.1% in near-wall convective heat transfer with the lower Fourier mode ($m = 3$) wall modification (see Figure 4.5b). In contrast, Case II and Case III generated greater inhibition to convective heat transfer with a maximum reduction of $\sim$9% in Nusselt number at the onset of the downstream section. This indicates to the capability of the targeted wall perturbations in reducing convective heat transfer, hence presenting feasibility to inhibit heat losses to ground rock formations in geothermal systems. Within a downstream region of $x = 2D - 10D$, the average inhibitions in near-wall convective heat transfer were 1.1%, 3.4%, and 3.2% for Case I, Case II, and Case III, respectively. It is worth indicating that the adopted wall modifications caused substantial changes in flow and heat transfer properties inside the pipe-insert section; however, the present study focuses on downstream variations and recovery of the thermal characteristics. Through a close inspection of Figure 4.5a, we noticed a self-similar thermal response and recovery for Case II and Case III. This self-similarity indicated to a predominant impact of the higher Fourier mode ($m = 15$) wall shape on manipulating the heat transfer characteristics and recovery. Further, a qualitative comparison between Figures 4.3a and 4.5a revealed that the distributions of Nu and C_f along the axial direction are well correlated. This was referred to the characteristic nature of forced-convection flows, which dictate the correlation between temperature and velocity gradients Ramgadia and Saha (2013). The results thus far clearly confirm the impacts of the targeted wall shapes on manipulating flow and thermal characteristics towards reducing convective heat transfer and frictional drag in the downstream zone, thus presenting capability to minimize heat losses to ground formations pertinent to geothermal applications with saving pumping power.

4.4 Summary

This chapter numerically examined the hydrodynamic and thermal characteristics of turbulent pipe flow experiencing sudden variations in wall geometry at Reynolds number of 7.5×10^4. The modified wall conditions were designed to best replicate particular azimuthal Fourier modes corresponding to $m = 3$, $m = 15$, and $m = 3 + 15$. The targeted wall perturbations generated long-lasting variations in flow and convective heat transfer properties in favor of mitigating heat losses to subsurface rock formations in geothermal systems with saving pumping power. This provided a potential approach towards increasing the efficiency of subsurface thermal systems. In response to the wall modifications, mean axial flow exhibited deceleration and reduced velocity gradients in near-wall region for all three cases. These modified flow characteristics contributed to local reduction in convective heat transfer, thus presenting the capability to suppress heat losses in geothermal applications. Particularly, the wall modifications of $m = 15$ and $m = 3 + 15$ resulted in a maximum decrease of $\sim$9% in convective heat transfer coefficient, immediately after the pipe-insert section compared to smooth-pipe flow at similar working conditions. The mean temperature profiles along the radial direction revealed a similar thermal response of the higher and combined Fourier modes ($m = 15$ and $m = 3 + 15$), such that the fully-developed thermal state was depicted at $x = 40D$ from the perturbation. The similarities in the modified thermal response and recovery obtained from $m = 15$ and $m = 3 + 15$ implied a profound impact by the higher Fourier mode on manipulating the heat transfer characteristics. The attenuation in convective heat transfer was accompanied by a substantial decrease ($\sim$17%) in skin friction and wall shear stress for the wall modifications of $m = 15$, and $m = 3 + 15$. The perturbed wall condition of $m = 3$ led to averaged reductions of $\sim$1.1% and $\sim$1.6% in near-wall convective heat transfer and frictional drag, respectively.

Chapter 5

EFFECTS OF REYNOLDS NUMBER

5.1 Introduction

Reynolds number effects on convective heat transfer characteristics and recovery of turbulent pipe flow hampered by abrupt wall changes are studied at a range of Reynolds numbers between 2.5×10^4 and 7.5×10^4. The thermal response is investigated by characterizing the mean flow and convective heat transfer properties in the wake region of pipe inserts.

A detailed review of literature on thermal responses to manipulation techniques in wall-bounded turbulent flows was presented in Sections 2.5 and 2.6. The results of Van Buren et al. (2017) and Masoumifar et al. (2021a) have confirmed that implementing pipe-inserts, resembling certain Fourier modes, caused substantial modifications in flow properties. These hydrodynamic changes resulted in favourable reductions in skin-friction drag and convective heat transfer in the downstream wake, as demonstrated in Chapter 4. Further, Masoumifar et al. (2021b) depicted strong impacts of Reynolds number on flow dynamics and recovery in the presence of these targeted wall shapes. However, a knowledge gap exists, where the implications of varying bulk Reynolds number on convective heat transfer properties have not been studied for turbulent pipe flow perturbed by abrupt surface variations mimicking distinct Fourier modes. Hence, this chapter

focuses on Reynolds-number implications on heat transfer response and recovery of turbulent pipe flow past targeted wall modifications, as previously outlined in Section 1.2.

This chapter addresses the last main objective (4) of this thesis, as outlined in Section 1.3. The chapter is organized such that a description of the problem is presented in Section 5.2. Presentation and discussion of the results are included in Section 5.3. The main findings are summarized in Section 5.4.

5.2   Problem Description

The bulk Reynolds number ranged between 2.5×10^4 and 7.5×10^4. The sudden variation in the pipe surface condition was introduced through deployment of a pipe-insert section, the geometrical shape of which was designed to closely mimic those of Van Buren et al. (2017) and Masoumifar et al. (2021b,a), as shown and described in Section 1.2. Among all wall modifications, the results elucidating Reynolds-number impacts are solely presented and discussed for Case II ($m = 15$) in this chapter. However, results of Case I and Case III depicted similar Reynolds number effects for all targeted wall shapes (Masoumifar et al., 2021b).

5.3   Results and Discussions

We start by investigating impacts of the targeted wall shape on radial distributions of mean streamwise (axial) velocity at several downstream locations within $x = 2D - 40D$ for $Re = 7.5 \times 10^4$, $Re = 4.0 \times 10^4$, and $Re = 2.5 \times 10^4$ in Figures 5.1(a-c). The mean streamwise velocity distributions are normalized using inlet bulk velocity (U_∞) and r/R symbolizes the non-dimensional radial coordinate. Variations in mean flow velocity were quantified by calculating local differences (Δ) from fully-developed condition. Here, the fully-developed state corresponds to flow and heat transfer characteristics at $x/D = 90$, where we observed no alterations in mean flow and heat transfer properties compared to smooth pipe flow at identical flow conditions. Immediately downstream of the pipe perturbation, the mean velocity profiles showed a velocity-deficit feature

(a)

(b)

(c)
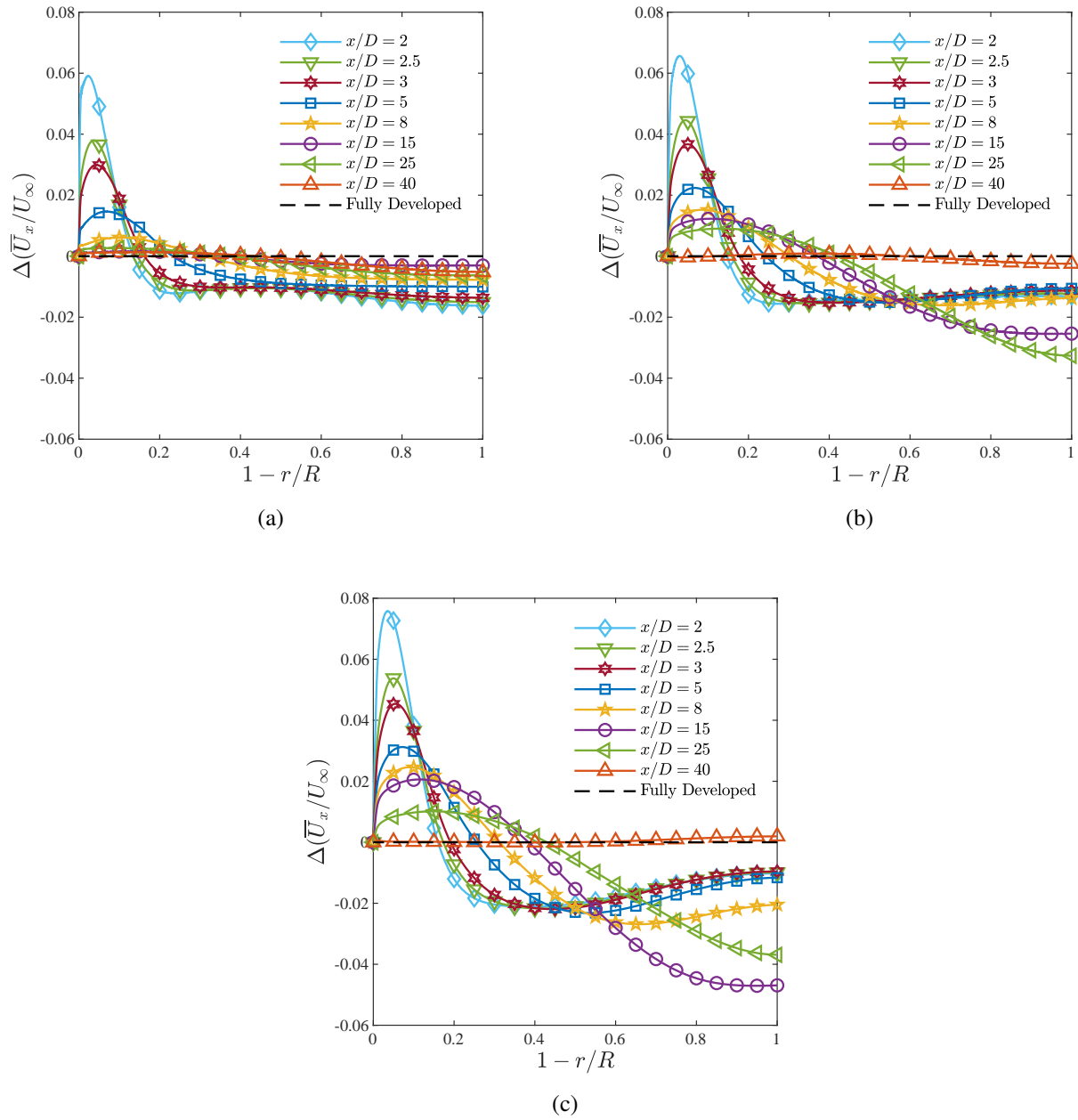
Figure 5.1: Mean streamwise velocity profile development for (a) $Re = 7.5 \times 10^4$, (b) $Re = 4.0 \times 10^4$, (c) $Re = 2.5 \times 10^4$.

in near-wall zone ($0 < 1 - r/R < 0.2$) for all examined Reynolds numbers. The velocity-deficit characteristic is depicted in Figure 5.1 where the variations (Δ) in local velocity overshoot above the fully-developed profile for all cases. Further, the flow appeared to accelerate in the core region by "pivoting" (Van Buren et al., 2020) around an intermediate point along the radial direction (r/R)

55

to balance the velocity deficit close to the wall. The flow acceleration in the core region, which compensated the deficit in velocity distribution close to the wall, was linked to the genuine nature of confined flows (e.g., pipe and channel flows) (Van Buren et al., 2020). For all Reynolds numbers, radial velocity profiles exhibited a mean-flow recovery process within the downstream zone of $x = 2D - 40D$, in which the mean flow accelerated and decelerated towards the fully relaxed condition in the near-wall and outer flow regions, respectively. These main flow observations agreed well with the experimental and numerical findings of Van Buren et al. (2017) and Masoumifar et al. (2021a,b). The downstream reduced-velocity flow ribbon implied lowering of radial velocity and temperature gradients within the near-wall region, thereby promoting a downstream zone of reduced drag and convective heat transfer for all Reynolds numbers considered here. From a practical point of view, the flow deceleration in the near-wall region hinted at the potential reduction of convective heat transfer process with a concurrent decrease in skin-friction drag (Castellanos et al., 2022). This could lead to suppression of heat losses in subsurface thermal systems (e.g., heat dissipation to ground rock formations in geothermal applications).

The radial variations of $\Delta(\overline{U_x}/U_\infty)$ at $x/D = 5$ for all considered Reynolds numbers are presented in Figure 5.2. The radial profiles of Figure 5.2 distinctly indicate substantial effects of
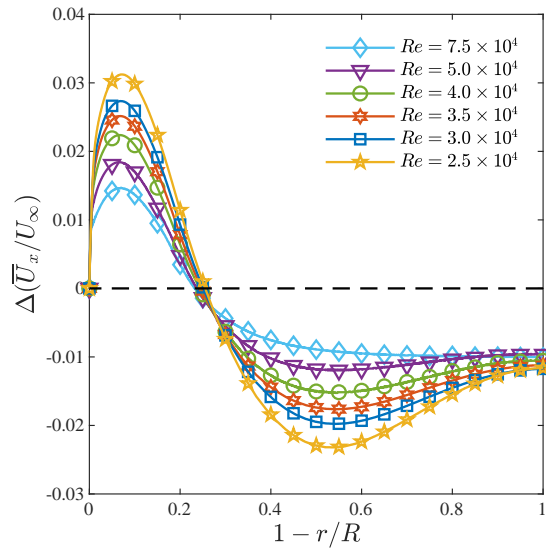

Figure 5.2: Radial variations of axial velocity at $x/D = 5$ for all examined Reynolds numbers.

varying Reynolds number on the mean flow response, downstream of the pipe insert. At highest Reynolds number ($Re = 7.5 \times 10^4$), the velocity profile showed a maximum velocity deficit of $\sim 1.5\%$ compared to fully-developed condition at a radial distance of $\approx 0.15R$ from the wall. Further, the peak of $\Delta(\overline{U_x}/U_\infty)$ was observed to increase in magnitude with decreasing Reynolds numbers within $0 < 1 - r/R < 0.3$, leading to a maximum reduction of $\sim 3\%$ in velocity profiles at the lowest Reynolds number ($Re = 2.5 \times 10^4$). The flow in the core region exhibited a similar trend with changing Reynolds numbers due to the balance of continuity. The increment in velocity deficit close to the wall indicates more reductions in convective heat transfer and skin-friction drag coefficients with decreasing Reynolds numbers within the examined range (Castellanos et al., 2022).

In order to explore the evolution of mean streamwise velocity in the outer (core) flow region, we looked at velocity profiles along the wake centreline for all considered Reynolds numbers in Figure 5.3. Here, the mean streamwise velocity is normalized by the maximum velocity magnitude from fully-developed distribution (U_b), and the axial location is normalized by the pipe diameter (D). In response to the targeted perturbation, the mean streamwise flow was noticed to locally accelerate along the wake centreline for the whole ambit of Reynolds numbers studied here. For
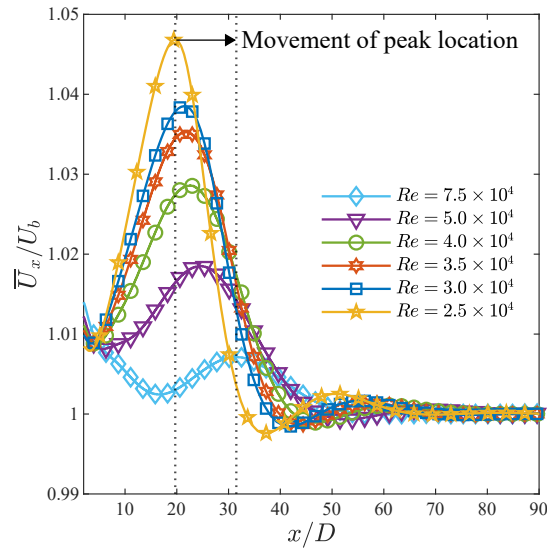

Figure 5.3: Variations of mean axial velocity along the wake centreline.

the highest Reynolds number, the axial variation of mean velocity depicted a peak at $x/D \approx 32$, with a magnitude $\sim 1\%$ higher than the fully-developed value. The accelerated flow was observed to slowly retrieve to the fully-developed state after this peak, leading to a prolong recovery process. The depicted oscillatory mean flow behavior and the extended recovery process imply the presence of non-monotonic flow trend in response to the targeted wall shape (Van Buren et al., 2017; Masoumifar et al., 2021a,b; Van Buren et al., 2020). This observation of mean flow along the wake centreline remains intact for all Reynolds numbers. However, the peak was observed to increase in magnitude, while its axial position shifted upstream towards the pipe perturbation with decreasing Reynolds numbers. The peak location (L_p) of $\overline{U_x}/U_b$ was quantitatively traced with varying Reynolds number and averaged Nusselt number in Figures 5.4a and 5.4b, respectively. It was found that the peak of $\overline{U_x}/U_b$ presented a power-law translation mode in the form of $Re^{0.4}$ and $Nu^{0.5}$. This indicated a relatively-faster recovery process of mean flow and heat transfer characteristics at lower Reynolds numbers. It also hinted to considerable Reynolds number effects on the hydrodynamic and thermal response in the downstream wake.
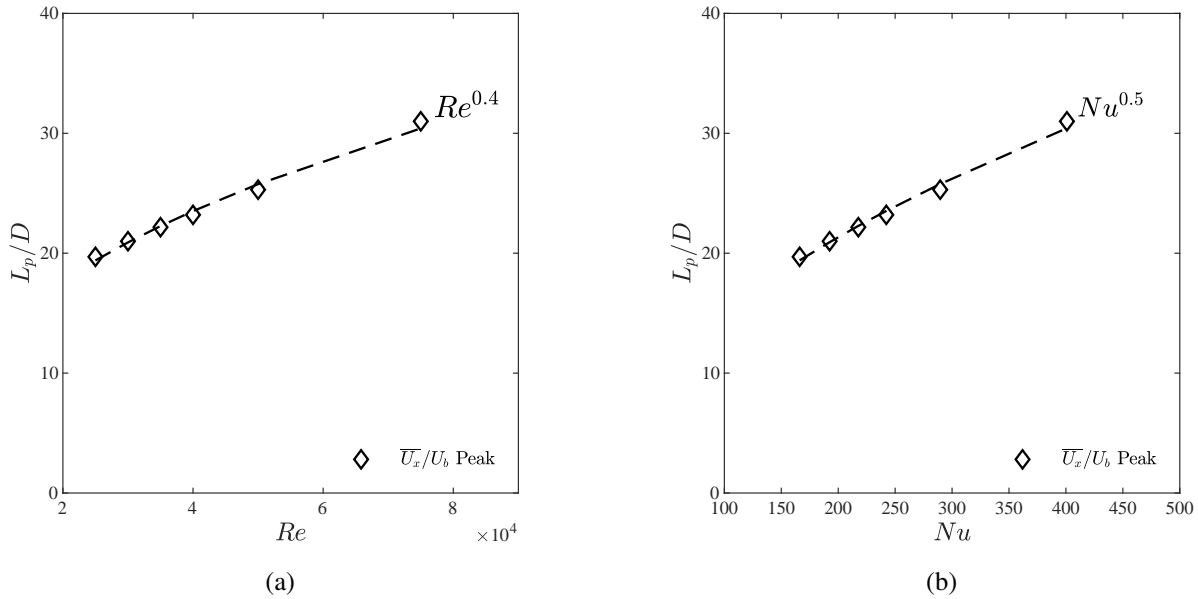

Figure 5.4: Variations of $\overline{U_x}/U_b$ peak location with respect to (a) Reynolds number, (b) averaged Nusselt number.

To more clearly illustrate the implications of bulk Reynolds numbers on convective heat transfer and frictional drag downstream of the pipe insert, Figures 5.5a and 5.5b depict the axial variations of local Nusselt number (Nu) and skin-friction coefficient (C_f), respectively. Both traced quantities were normalized by the fully-developed values (Nu_b and $C_{f,b}$) calculated at the farthest downstream position ($x/D = 90$). For all examined Reynolds numbers, we observed an abrupt initial drop in the axial distributions of Nu and C_f below fully-developed level, thereby indicating the capability of the targeted geometric perturbation in inhibiting dissipation of fluid thermal energy to surroundings and reducing frictional drag. The immediate decrease of convective heat transfer and frictional drag was then followed by a relaxation behaviour towards fully-developed condition within $2D - 40D$ for all Reynolds numbers. The presented reductions in convective heat transfer and frictional drag were attributed to the formation of near-wall downstream ribbon of reduced-momentum flow, which was previously depicted in Figure 5.1 as deficit in velocity profiles close to the pipe wall. The generation of low-momentum flow in the near-wall region was identified previously as a flow mechanism to successfully reduce skin-friction drag (Schoppa and Hussain, 1998; Cheng et al., 2021; Whalley and Choi, 2014; Du et al., 2002). Analogously, this was more
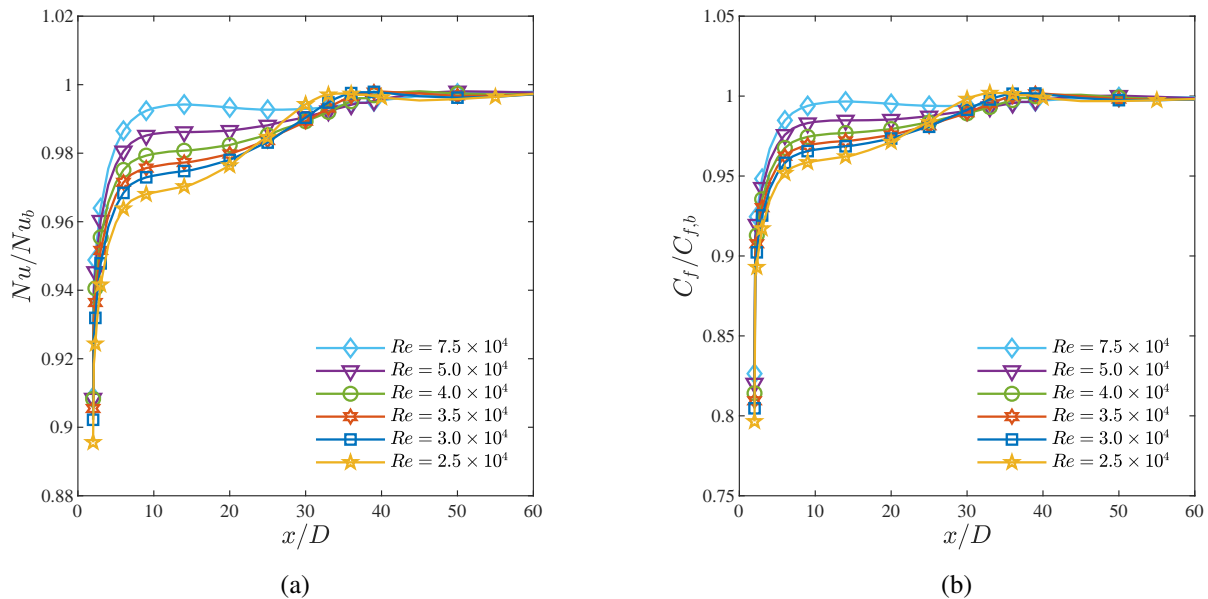

Figure 5.5: Variations of (a) Nusselt number, (b) skin-friction coefficient, in the downstream wake.

Table 5.1: Averaged reductions in Nusselt number and skin-friction coefficient within $x = 2D - 10D$ compared to the highest Re case.

Re	Nu/Nu_b	$C_f/C_{f,b}$	$\Delta(Nu)_{Re}$	$\Delta(C_f)_{Re}$
7.5×10^4	3.38%	5.03%		
5.0×10^4	3.85%	5.75%	0.46%	0.72%
4.0×10^4	4.33%	6.49%	0.95%	1.46%
3.5×10^4	4.71\$	7.01%	1.32%	1.98%
3.0×10^4	5.07%	7.46%	1.68%	2.43%
2.5×10^4	5.67%	8.25%	2.29%	3.22%

recently reported as an efficient strategy to mitigate convective heat transfer (Castellanos et al., 2022). In response to the existence of pipe insert, the maximum reductions of convective heat transfer and frictional drag were quantified as ∼9.2% and ∼17.4%, respectively, for the highest Reynolds number ($Re = 7.5 \times 10^4$) compared to smooth pipe flow at identical flow conditions. The averaged reductions in heat convection and frictional drag within $x = 2D - 10D$ were quantified as 3.4% and 5.0% for $Re = 7.5 \times 10^4$, respectively. However, the reductions in Nu and C_f were observed to increase in magnitude with decreasing bulk Reynolds numbers. Table 5.1 outlines the averaged reductions in Nu and C_f within $x = 2D - 10D$ and their percentage differences with respect to the corresponding averaged reduction obtained from the highest Reynolds number. Results clearly demonstrate that an additional attenuation of ∼2.3% in convective heat transfer was achieved within $x = 2D - 10D$ with decreasing Re from 7.5×10^4 to 2.5×10^4, corresponding to an averaged reduction of ∼5.7% at $Re = 2.5 \times 10^4$ compared to smooth pipe condition. Similarly, a further reduction of 3.2% in C_f was obtained with the decrease of Re from 7.5×10^4 to 2.5×10^4, corresponding to an averaged decrease of ∼8.3% at $Re = 2.5 \times 10^4$ compared to smooth wall condition. These higher reductions were linked to the additional velocity deficit associated with decreasing Re as presented in Figure 5.2. The qualitative resemblance between the axial distributions of local Nusselt number and skin-friction coefficient in the downstream wake (shown in Figure 5.5) supports the existence of a correlation between heat flux and wall shear stress in wall-bounded flows. This agrees well with Reynolds analogy, which suggests that the flow manip-

ulations that target reductions in frictional drag can concurrently contribute in favorable inhibition of convective heat transfer (Castellanos et al., 2022).

We further looked at radial changes of mean temperature compared to fully developed distribution in Figure 5.6 within $x = 2D - 40D$ for $Re = 7.5 \times 10^4$ and $Re = 2.5 \times 10^4$. Here, the mean temperature is normalized by friction temperature ($T_\tau = q_w / \rho C_p u_\tau$) and $r^+ = r u_\tau / \nu$ denotes the normalized radial distance. For all Reynolds numbers, we observed a significant increment in magnitude of flow temperature above the fully-developed state along the radial distance ($r^+ > 10$), immediately after the pipe insert. This was attributed to the contributions of the targeted pipe modification in inhibiting convective heat transfer and heat fluxes near the pipe wall. The initial increase of fluid temperature was then preceded by a relaxation trend, in which mean temperature profiles approached fully relaxed state within $x = 2D - 40D$. A close examination of the temperature profiles for the highest Reynolds number revealed that the fully developed condition was slowly recovered at an axial location of $x/D = 40$, thereby hinting at a delayed recovery behaviour of fully-developed heat transfer mechanism at higher Reynolds numbers. This was attributed to the
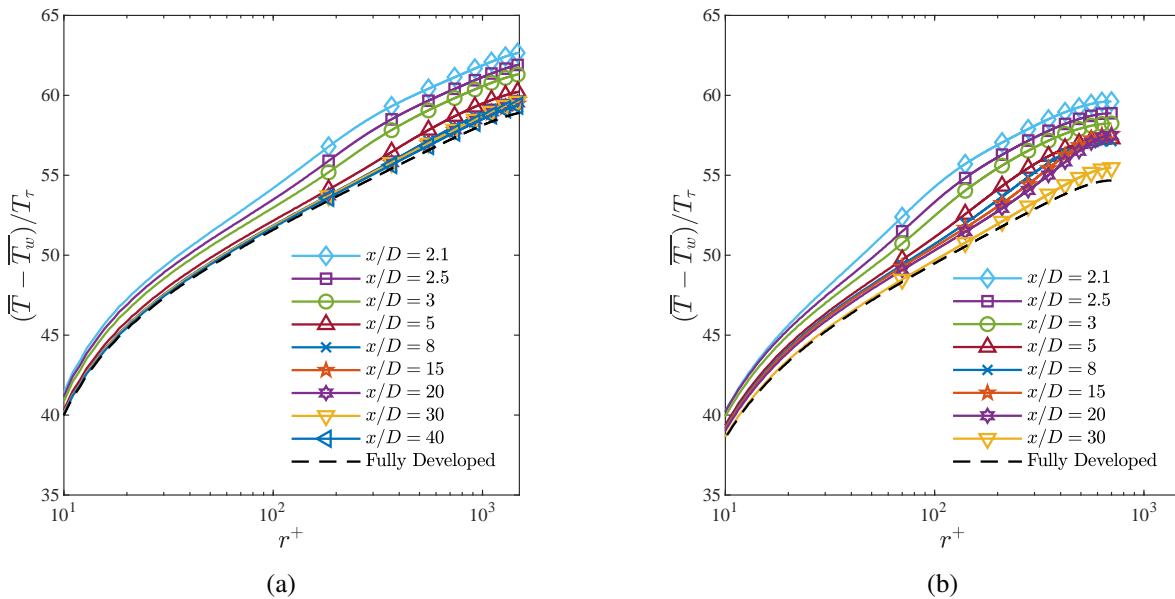

Figure 5.6: Mean temperature profile development for (a) $Re = 7.5 \times 10^4$, (b) $Re = 2.5 \times 10^4$.

existence of non-monotonic (oscillatory) flow response to the pipe perturbation in the downstream wake.

Recovery of mean flow and heat transfer properties can be best assessed by tracing the axial locations where the dimensionless velocity and temperature profiles appear to retrieve the fully-developed conditions. Figure 5.7 quantitatively evaluates the normalized location of recovery (L_r/D) for the entire range of bulk Reynolds numbers examined here. These recovery locations were determined based on a maximum percentage difference of less than 0.5% for the dimensionless velocity and temperature profiles compared to the fully-developed condition at $x/D = 90$. These results clearly elucidate that increasing Reynolds number caused a delay in retrieving the fully-developed mean flow and heat transfer characteristics, thus leading to an extension to the axial recovery zone. This observation agreed well with the recovery behaviour preceding targeted Fourier mode perturbation, depicted by Masoumifar et al. (2021b). We further observed that the variations in the recovery length approached an asymptotic trend at $Re \geq 5.0 \times 10^4$, where the changes in L_r/D were less than 1% compared to the highest Reynolds number case. A close in-
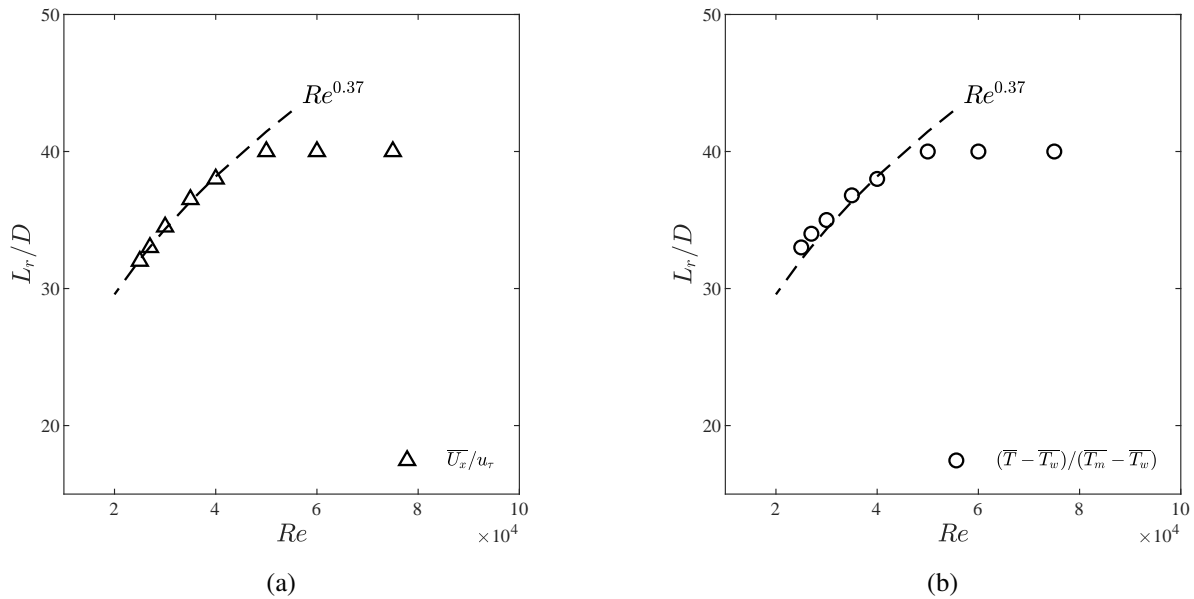

Figure 5.7: Variation of the recovery length at a range of Reynolds number (a) dimensionless velocity profiles, (b) dimensionless temperature profiles.

spection of Figures 5.7a and 5.7b revealed small variations in the recovery lengths of mean velocity and temperature profiles, which implied that the mean flow and heat transfer mechanisms were recovered concurrently. This further indicated that heat transfer recovery is mainly dominated by the recovery of mean flow in the downstream wake, which was attributed to the existence of a correlation between velocity and temperature gradients in forced convective flows (Ramgadia and Saha, 2013). The results in Figures 5.7a and 5.7b, particularly, demonstrate that the axial recovery length can be modeled as $Re^{0.37}$ for both mean velocity and temperature properties.

Fully developed (fully recovered) distributions of mean streamwise velocity at $x/D = 90$ are analyzed for all examined Reynolds numbers in Figure 5.8a. The axial flow appeared to speed up close to the pipe wall and slow down in the core flow region with increasing Re. This can be linked to the impact of turbulence on conveying high-momentum flow towards the pipe walls, as formerly stated by Malin (1997). Further, it was observed that the location where the bulk velocity matches the mean velocity exists at $r/R = 0.25$ from the wall, an observation that remains intact with varying Reynolds number. These trends agreed well with those of Zagarola and Smits (1998)
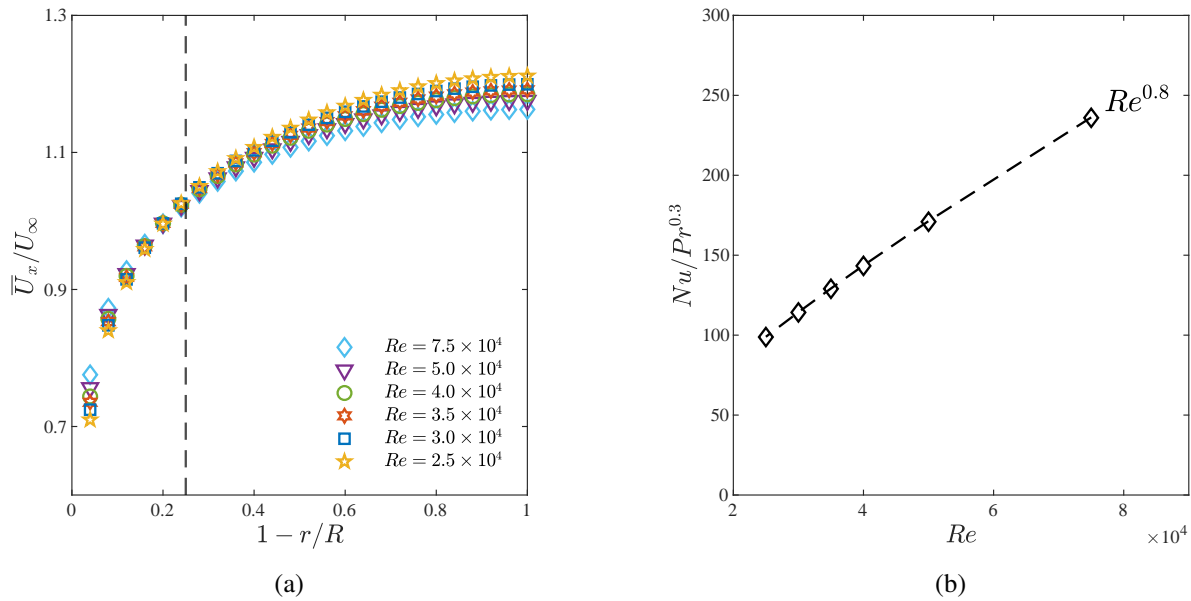

Figure 5.8: Comparison of fully recovered fully developed (a) velocity profiles, (b) Nusselt numbers, for all Reynolds numbers.

and Furuichi et al. (2015). Figure 5.8b presents the variations of fully-developed Nusselt number at $x/D = 90$ for the entire range of Re. An increasing trend is depicted with increasing Reynolds numbers with a power-law mode following $Re^{0.8}$. This is consistent with the empirical correlation of Dittus–Boelter ($Nu \propto Re^{0.8} Pr^{0.3}$) for smooth turbulent pipeflows (Bergman et al., 2011).

This chapter thoroughly examined the implications of varying Reynolds number on thermal response and recovery of turbulent pipe flow past wall modification of Case II. Case I and Case III exhibit similar impacts of Reynolds number, as confirmed by Masoumifar et al. (2021b). The thermal implications of Fourier mode inserts were detailed in Chapter 4.

The findings of this chapter clearly indicate substantial Reynolds number effects on convective heat transfer implications and recovery in the presence of targeted wall modification. The results further hint at the feasibility of deploying a sudden change in wall geometry, targeting a particular Fourier mode of $m = 15$, as a means to concurrently mitigate convective heat transfer and frictional drag. This could suppress heat dissipation to ground rock formations in subsurface thermal applications with saving pumping power, hence presenting economical and ecological benefits.

5.4   Summary

The impacts of varying bulk Reynolds number on convective heat transfer characteristics of turbulent pipe flow impeded by sudden changes in wall geometry were examined numerically at a range of Reynolds numbers between 2.5×10^4 and 7.5×10^4. The results elucidated that deployment of the targeted wall modification caused momentum-deficit and reduced velocity gradients close to the pipe wall, downstream of the pipe-insert segment. The generation of near-wall downstream ribbon of reduced-velocity flow was viewed as flow mechanism to effectively attenuate convective heat transfer and frictional drag. Particularly, the results revealed that the maximum averaged reductions of ~5.7% and ~8.3% in convective heat transfer and frictional drag were obtained at $Re = 2.5 \times 10^4$ within a downstream region of $x = 2D - 10D$. Further, recovery behaviour of convective heat transfer was quantitatively investigated by tracking the changes in mean

dimensionless temperature after the pipe-insert segment. The results demonstrated that increasing the bulk Reynolds number resulted in slow recovery of the heat transfer properties towards the fully-developed condition, leading to a longer recovery length. The variations in recovery length exhibited an asymptotic behaviour for $Re \geq 5.0 \times 10^4$. The recovery length scaled with $Re^{0.37}$ for both mean velocity and temperature.

Chapter 6

CONCLUSION

This study focused on characterizing the thermal response and recovery of turbulent pipeflow hampered by targeted pipe-inserts using RANS-based SST $k - \omega$ turbulence model at a range of Reynolds numbers, $Re = 2.5 \times 10^4 - 7.5 \times 10^4$. In particular, this dissertation first looked at heat transfer implications of abrupt wall changes resembling particular Fourier modes, $m = 3$, $m = 15$, and $m = 3 + 15$, at the highest Reynolds number of $Re = 7.5 \times 10^4$. Then, the study was extended to examine effects of varying bulk Reynolds number on thermal response and recovery in the presence of targeted wall modifications. This investigation further analyzed variations in skin-frictional drag of turbulent pipeflow due to the implementation of these wall shapes.

The current study introduced a novel pipe flow manipulation mechanism that targets the extraction and harvesting of energy using subsurface thermal systems with suppressed heat losses and minimal pumping power requirement. Particularly, this dissertation quantitatively demonstrated that deployment of the targeted pipe-inserts yield desirable reductions in near-wall heat convection and frictional drag. The final design would incorporate intermittent placement of optimized-shape pipe-inserts at fixed intervals to substantially enhance the efficiency of subsurface thermal systems. An extensive validation study was performed to assess the performance of SST $k - \omega$ turbulence model in adequately predicting the mean flow and heat transfer features, which closely agreed with available experimental data.

Impacts of the targeted changes in wall shape on thermal response and recovery were investigated at Reynolds number of 7.5×10^4. For all three cases, and immediately downstream of the pipe-inserts, the mean flow appeared to decelerate (momentum-deficit) close to the pipe wall, implying local reductions in velocity gradients. The velocity-deficit was recompensed as acceleration of mean streamwise velocity in the core flow region, which was attributed to the characteristic flow dynamics in wall-bounded domains (e.g., pipes and channels) (Van Buren et al., 2019). The flow deceleration in the near-wall region and flow acceleration along the wake centerline established the capacity of Fourier pipe-inserts in manipulating pipeflow dynamics. Inspections of axial velocity variations along the wake centerline revealed the existence of a peak at a downstream location of $x/D = 32$ for all targeted perturbations, which hinted at characteristics of non-monotonic (oscillatory) flow response at the examined Reynolds number ($Re = 7.5 \times 10^4$). The formation of reduced-momentum flow close to the wall led to attenuation in near-wall convective heat transfer and skin-frictional drag. The axial variations of Nusselt number and skin-friction coefficient depicted an initial abrupt drop in magnitude, before relaxing towards fully-developed pipeflow conditions. In particular, the pipe perturbations of $m = 15$ and $m = 3 + 15$ resulted in a maximum reduction of $\sim 9\%$ in near-wall convective heat transfer, immediately past the pipe-insert section. This was escorted by reductions in frictional drag, which quantified as $\sim 17.4\%$ and $\sim 16.5\%$ for wall modifications of $m = 15$ and $m = 3 + 15$, respectively. Further, within a downstream zone of $2D - 10D$, the maximum averaged reductions in heat transfer and frictional drag were reported for the wall shape of $m = 15$, corresponding to 3.4% and 5.0%, respectively. Recovery of heat transfer was quantitatively examined by comparing radial distributions of dimensionless mean temperature with fully-developed thermal condition. A similar prolong recovery process was illustrated for perturbation shapes of higher $m = 15$ and superimposed ($m = 3 + 15$) Fourier modes, such that the fully-developed thermal condition was retrieved at $x/D = 40$ after the pipe insert. The wall perturbation of $m = 3$ resulted in averaged decrease of 1.1% and 1.6% in convective heat transfer and frictional drag characteristics, respectively.

Reynolds number effects on convective heat transfer characteristics were investigated for turbulent pipeflow perturbed by pipe-insert mimicking the higher Fourier mode of $m = 15$. Results indicated velocity-deficit characteristic in the near-wall region for all examined Reynolds numbers. The deficit in velocity profiles was noted to increase in magnitude with deceasing Reynolds number, compared to fully-developed pipeflow condition. The mean flow response along the wake centerline depicted a peak, whose axial position was found to follow a power-law shifting course in the form of $L_p/D \propto Re^{0.4}$ and $L_p/D \propto Nu^{0.5}$. The deficit in velocity profiles close to the wall contributed to concurrent inhibitions to near-wall convective heat transfer and frictional drag. The maximum reductions of ~10.5% and ~20.5% in near-wall convective heat transfer and skin-frictional drag were depicted at the lowest Reynolds number case ($Re = 2.5 \times 10^4$), corresponding to averaged reductions of 5.7% and 8.3%, respectively. Recovery analysis of convective heat transfer revealed that increasing bulk Reynolds number resulted in a delayed recovery process towards the fully-developed thermal state, leading to an extended recovery length. The overall recovery length depicted an asymptotic trend for $Re \geq 5.0 \times 10^4$. The recovery position was scaled with $Re^{0.37}$ for both mean velocity and temperature characteristics.

6.1 Future Work

The outcomes of this dissertation present a framework to enrich our cumulative knowledge and understanding on thermal implications of perturbed turbulent pipeflows. While a thorough investigation was introduced on characterization of thermal response and recovery past Fourier pipe-inserts, remaining unchallenged questions still require further examinations, particularly:

1. Implications of distinct geometric parameters on thermal response and recovery, including perturbation thickness and pipe-insert length.

2. Impacts of multiple Fourier pipe-inserts and separation distance on thermal response and recovery.

3. Studying the implications of non-Newtonian flow characteristics on thermal response and recovery past these targeted pipe-inserts.

4. Implication of multiphase flow features on thermal response and recovery.

5. Investigation of the detailed turbulent flow and convective heat transfer fields using Direct Numerical Simulations at moderate Reynolds numbers.

6. Reynolds number scaling of thermal response and recovery past Fourier pipe perturbations, including laminar, transitional, and turbulent flow regimes.

7. The effects of Fourier pipe-inserts on structural stresses and flow-induced vibrations for optimizing their design and installation practices.

Bibliography

Alam, T. and Kim, M.-H. (2018). A comprehensive review on single phase heat transfer enhancement techniques in heat exchanger applications. *Renewable and Sustainable Energy Reviews*, 81:813–839.

Aljallis, E., Sarshar, M. A., Datla, R., Sikka, V., Jones, A., and Choi, C.-H. (2013). Experimental study of skin friction drag reduction on superhydrophobic flat plates in high reynolds number boundary layer flow. *Physics of fluids*, 25(2):025103.

Anderson, W., Barros, J. M., Christensen, K. T., and Awasthi, A. (2015). Numerical and experimental study of mechanisms responsible for turbulent secondary flows in boundary layer flows over spanwise heterogeneous roughness. *Journal of Fluid Mechanics*, 768:316–347.

Batchelor, G. K. (2000). *An Introduction to Fluid Dynamics*. Cambridge Mathematical Library. Cambridge University Press.

Bayer, P., Rybach, L., Blum, P., and Brauchler, R. (2013). Review on life cycle environmental effects of geothermal power generation. *Renewable and Sustainable Energy Reviews*, 26:446–463.

Bechert, D., Bruse, M., Hage, W. v., Van der Hoeven, J. T., and Hoppe, G. (1997). Experiments on drag-reducing surfaces and their optimization with an adjustable geometry. *Journal of fluid mechanics*, 338:59–87.

Bergman, T. L., Lavine, A. S., Incropera, F. P., and DeWitt, D. P. (2011). *Introduction to heat transfer*. John Wiley & Sons.

Berner, C., Durst, F., and McEligot, D. (1984). Flow around baffles.

Bertani, R. (2012). Geothermal power generation in the world 2005–2010 update report. *geothermics*, 41:1–29.

Bushnell, D. M. (1990). *Viscous drag reduction in boundary layers*, volume 123. AIAA.

Cappelli, D. and Mansour, N. N. (2013). Performance of reynolds averaged navier-stokes models in predicting separated flows: Study of the hump flow model problem. In *31st AIAA Applied Aerodynamics Conference*, page 3154.

Cassie, A. and Baxter, S. (1944). Wettability of porous surfaces. *Transactions of the Faraday society*, 40:546–551.

Castellanos, R., Michelis, T., Discetti, S., Ianiro, A., and Kotsonis, M. (2022). Reducing turbulent convective heat transfer with streamwise plasma vortex generators. *Experimental Thermal and Fluid Science*, page 110596.

Cha, T.-G., Yi, J. W., Moon, M.-W., Lee, K.-R., and Kim, H.-Y. (2010). Nanoscale patterning of microtextured surfaces to control superhydrophobic robustness. *Langmuir*, 26(11):8319–8326.

Chaube, A., Sahoo, P., and Solanki, S. (2006). Analysis of heat transfer augmentation and flow characteristics due to rib roughness over absorber plate of a solar air heater. *Renewable Energy*, 31(3):317–331.

Checco, A., Ocko, B. M., Rahman, A., Black, C. T., Tasinkevych, M., Giacomello, A., and Dietrich, S. (2014). Collapse and reversibility of the superhydrophobic state on nanotextured surfaces. *Physical Review Letters*, 112(21):216101.

Cheng, X., Wong, C., Hussain, F., Schröder, W., and Zhou, Y. (2021). Flat plate drag reduction using plasma-generated streamwise vortices. *Journal of Fluid Mechanics*, 918.

Choi, H., Moin, P., and Kim, J. (1993). Direct numerical simulation of turbulent flow over riblets. *Journal of fluid mechanics*, 255:503–539.

Choi, H. S. and Suzuki, K. (2005). Large eddy simulation of turbulent flow and heat transfer in a channel with one wavy wall. *International journal of heat and fluid flow*, 26(5):681–694.

Churchill, S. W. (2002). A reinterpretation of the turbulent prandtl number. *Industrial & engineering chemistry research*, 41(25):6393–6401.

Corke, T. C. and Thomas, F. O. (2018). Active and passive turbulent boundary-layer drag reduction. *AIAA journal*, 56(10):3835–3847.

Costantini, R., Mollicone, J.-P., and Battista, F. (2018). Drag reduction induced by superhydrophobic surfaces in turbulent pipe flow. *Physics of Fluids*, 30(2):025102.

Daniello, R. J., Waterhouse, N. E., and Rothstein, J. P. (2009). Drag reduction in turbulent flows over superhydrophobic surfaces. *Physics of Fluids*, 21(8):085103.

Davidson, L. et al. (2018). Fluid mechanics, turbulent flow and turbulence modeling. *Chalmers University of Technology, Goteborg, Sweden (Nov 2011)*.

Den Toonder, J. and Nieuwstadt, F. (1997). Reynolds number effects in a turbulent pipe flow for low to moderate re. *Physics of Fluids*, 9(11):3398–3409.

DiPippo, R. and Renner, J. L. (2014). Geothermal energy. In *Future Energy*, pages 471–492. Elsevier.

Du, Y., Symeonidis, V., and Karniadakis, G. E. (2002). Drag reduction in wall-bounded turbulence via a transverse travelling wave. *Journal of fluid mechanics*, 457:1–34.

Durst, F. and Wang, A.-B. (1989). Experimental and numerical investigations of the axisymmetric, turbulent pipe flow over a wall-mounted thin obstacle. In *7th Symposium on Turbulent Shear Flows, Volume 1*, volume 1, pages 10–4.

Eiamsa-ard, S. and Changcharoen, W. (2011). Analysis of turbulent heat transfer and fluid flow in channels with various ribbed internal surfaces. *Journal of Thermal Science*, 20(3):260–267.

Elders, W. and Moore, J. (2016). Geology of geothermal resources. *Geothermal Power Generation*, pages 7–32.

Fuaad, P. and Prakash, K. A. (2017). Influence of texture on thermal transport in streamwise-aligned superhydrophobic turbulent channels. *International Journal of Thermal Sciences*, 114:72–85.

Furuichi, N., Terao, Y., Wada, Y., and Tsuji, Y. (2015). Friction factor and mean velocity profile for pipe flow at high reynolds numbers. *Physics of Fluids*, 27(9):095108.

Gajusingh, S. T., Shaikh, N., and Siddiqui, K. (2010). Influence of a rectangular baffle on the downstream flow structure. *Experimental Thermal and Fluid Science*, 34(5):590–602.

Garcia-Mayoral, R. and Jiménez, J. (2011). Drag reduction by riblets. *Philosophical transactions of the Royal society A: Mathematical, physical and engineering Sciences*, 369(1940):1412–1427.

Garrett-Peltier, H. (2017). Green versus brown: Comparing the employment impacts of energy efficiency, renewable energy, and fossil fuels using an input-output model. *Economic Modelling*, 61:439–447.

George, W. K. (2013). Lectures in turbulence for the 21st century. *Chalmers University of Technology*, 550.

Goldstein Jr, L. and Sparrow, E. M. (1977). Heat/mass transfer characteristics for flow in a corrugated wall channel.

Goswami, S. and Hemmati, A. (2020). Response of turbulent pipeflow to multiple square bar roughness elements at high reynolds number. *Physics of Fluids*, 32(7):075110.

Goswami, S. and Hemmati, A. (2021). Evolution of turbulent pipe flow recovery over a square bar roughness element at a range of reynolds numbers. *Physics of Fluids*, 33(3):035113.

Greenshields, C. J. et al. (2015). Openfoam user guide. *OpenFOAM Foundation Ltd, version*, 3(1):47.

Günther, M. and Hellmann, T. (2017). International environmental agreements for local and global pollution. *Journal of Environmental Economics and Management*, 81:38–58.

Guo, Z., Li, D., and Wang, B. (1998). A novel concept for convective heat transfer enhancement. *International Journal of Heat and Mass Transfer*, 41(14):2221–2225.

Habib, M., Attya, A., and McEligot, D. (1988). Calculation of turbulent flow and heat transfer in channels with streamwise-periodic flow.

Hamilton, J. M., Kim, J., and Waleffe, F. (1995). Regeneration mechanisms of near-wall turbulence structures. *Journal of Fluid Mechanics*, 287:317–348.

Hu, X., Banks, J., Guo, Y., and Liu, W. V. (2022). Utilizing geothermal energy from enhanced geothermal systems as a heat source for oil sands separation: A numerical evaluation. *Energy*, 238:121676.

Hultmark, M., Vallikivi, M., Bailey, S. C. C., and Smits, A. (2013). Logarithmic scaling of turbulence in smooth-and rough-wall pipe flow. *Journal of Fluid Mechanics*, 728:376–395.

Hwang, R. R., Chow, Y.-C., and Peng, Y. (1999). Numerical study of turbulent flow over two-dimensional surface-mounted ribs in a channel. *International Journal for Numerical Methods in Fluids*, 31(4):767–785.

Jaluria, Y. and Torrance, K. E. (2017). *Computational heat transfer*. Routledge.

Jiménez, J. (2004). Turbulent flows over rough walls. *Annu. Rev. Fluid Mech.*, 36:173–196.

Jin, Y. and Herwig, H. (2014). Turbulent flow and heat transfer in channels with shark skin surfaces: Entropy generation and its physical significance. *International Journal of Heat and Mass Transfer*, 70:10–22.

Johansson, T. B. and Goldemberg, J. (2002). Energy for sustainable development: a policy agenda.

John, D. A. and Anderson, D. (2003). Modern compressible flow.

Johnston, I., Narsilio, G., and Colls, S. (2011). Emerging geothermal energy technologies. *KSCE Journal of Civil Engineering*, 15(4):643–653.

Joshi, J. and Nayak, A. K. (2019). *Advances of computational fluid Dynamics in nuclear reactor design and safety assessment*. Woodhead Publishing.

Kakac, S., Yener, Y., and Pramuanjaroenkij, A. (1995). *Convective heat transfer*, volume 2. CRC press Boca Raton.

Khaboshan, H. N. and Nazif, H. R. (2018). The effect of multi-longitudinal vortex generation on turbulent convective heat transfer within alternating elliptical axis tubes with various alternative angles. *Case studies in thermal engineering*, 12:237–247.

Kolmogorov, A. N. (1941). Equations of turbulent motion in an incompressible fluid. In *Dokl. Akad. Nauk SSSR*, volume 30, pages 299–303.

Kongkaitpaiboon, V., Promthaisong, P., Chuwattanakul, V., Wongcharee, K., and Eiamsa-ard, S. (2019). Effects of spiral start number and depth ratio of corrugated tube on flow and heat transfer characteristics in turbulent flow region. *Journal of Mechanical Science and Technology*, 33(8):4005–4012.

Kruse, N., GÜnther, A., and Von Rohr, P. R. (2003). Dynamics of large-scale structures in turbulent flow over a wavy wall. *Journal of Fluid Mechanics*, 485:87–96.

Kruse, N. and Von Rohr, P. R. (2006). Structure of turbulent heat flux in a flow over a heated wavy wall. *International journal of heat and mass transfer*, 49(19-20):3514–3529.

Kuethe, A. M. (1976). Foundations of aerodynamics: bases of aerodynamic design. *University of Michigan, USA, John Wiley & Sons, New York, Printed in the USA, ISBN: 0-471-50953-1.*

Kuhn, S., Kenjereš, S., and von Rohr, P. R. (2010). Large eddy simulations of wall heat transfer and coherent structures in mixed convection over a wavy wall. *International journal of thermal sciences*, 49(7):1209–1226.

Kumari, W. and Ranjith, P. (2019). Sustainable development of enhanced geothermal systems based on geotechnical research–a review. *Earth-Science Reviews*, 199:102955.

Lee, C. and Kim, C.-J. 2009). Maximizing the giant liquid slip on superhydrophobic microstructures by nanostructuring their sidewalls. *Langmuir*, 25(21):12812–12818.

Li, B., Feng, B., He, Y.-L., and Tao, W.-Q. (2006). Experimental study on friction factor and numerical simulation on flow and heat transfer in an alternating elliptical axis tube. *Applied Thermal Engineering*, 26(17-18):2336–2344.

Liu, S. and Sakr, M. (2013). A comprehensive review on passive heat transfer enhancements in pipe exchangers. *Renewable and sustainable energy reviews*, 19:64–81.

Lu, B. and Jiang, P.-X. (2006). Experimental and numerical investigation of convection heat transfer in a rectangular channel with angled ribs. *Experimental Thermal and Fluid Science*, 30(6):513–521.

Lumley, J. and Blossey, P. (1998). Control of turbulence. *Annual Review of Fluid Mechanics*, 30(1):311–327.

Lv, F. and Zhang, P. (2016). Drag reduction and heat transfer characteristics of water flow through the tubes with superhydrophobic surfaces. *Energy Conversion and Management*, 113:165–176.

Malin, M. (1997). Turbulent pipe flow of power-law fluids. *International communications in heat and mass transfer*, 24(7):977–988.

Manglik, R. (2003). Heat transfer enhancement. *Heat transfer handbook*, pages 1029–1130.

Masoumifar, M., Verma, S., and Hemmati, A. (2021a). Effects of targeted wall geometries on response of turbulent pipe flow at high reynolds number. *International Journal of Heat and Fluid Flow*, 92:108882.

Masoumifar, M., Verma, S., and Hemmati, A. (2021b). Response of turbulent pipe flow to targeted wall shapes at a range of reynolds numbers. *Physics of Fluids*, 33(6):065105.

Mckeon, B. J., Li, J.-d., Jiang, W., Morrison, J. F., and Smits, A. J. (2004). Further observations on the mean velocity distribution in fully developed pipe flow. *Journal of Fluid Mechanics*, 501:135–147.

Mead, I. (2017). International energy outlook 2017. *US Energy InformationAdministration*.

Meng, J. (2003). Enhanced heat transfer technology of longitudinal vortices based on field-coordination principle and its application. *Power Engineering and Engineering Thermophysics, Tsinghua University, Beijing*.

Meng, J.-A., Liang, X.-G., Chen, Z.-J., and Li, Z.-X. (2005). Experimental study on convective heat transfer in alternating elliptical axis tubes. *Experimental Thermal and Fluid Science*, 29(4):457–465.

Menni, Y., Azzi, A., and Chamkha, A. (2019). Enhancement of convective heat transfer in smooth air channels with wall-mounted obstacles in the flow path. *Journal of Thermal Analysis and Calorimetry*, 135(4):1951–1976.

Menter, F. (1993). Zonal two equation kw turbulence models for aerodynamic flows. In *23rd fluid dynamics, plasmadynamics, and lasers conference*, page 2906.

Menter, F. and Esch, T. (2001). Elements of industrial heat transfer predictions. In *16th Brazilian Congress of Mechanical Engineering (COBEM)*, volume 109, page 650.

Menter, F. R. (1992). Influence of freestream values on k-omega turbulence model predictions. *AIAA journal*, 30(6):1657–1659.

Naterer, G. F. (2018). *Advanced heat transfer*. CRC Press.

Ničeno, B. and Nobile, E. (2001). Numerical analysis of fluid flow and heat transfer in periodic wavy channels. *International Journal of Heat and Fluid Flow*, 22(2):156–167.

OpenCFD, O. (2019). The open source computational fluid dynamics (cfd) toolbox.

Park, H., Park, H., and Kim, J. (2013). A numerical study of the effects of superhydrophobic surface on skin-friction drag in turbulent channel flow. *Physics of Fluids*, 25(11):110815.

Park, H., Sun, G., et al. (2014). Superhydrophobic turbulent drag reduction as a function of surface grating parameters. *Journal of Fluid Mechanics*, 747:722–734.

Patankar, S., Liu, C., and Sparrow, E. (1977). Fully developed flow and heat transfer in ducts having streamwise-periodic variations of cross-sectional area.

Perkins, H. (1970). The formation of streamwise vorticity in turbulent flow. *Journal of Fluid Mechanics*, 44(4):721–740.

Petukhov, B. S. (1970). Heat transfer and friction in turbulent pipe flow with variable physical properties. In *Advances in heat transfer*, volume 6, pages 503–564. Elsevier.

Phuoc, T. X., Massoudi, M., Wang, P., and McKoy, M. L. (2019). Heat losses associated with the upward flow of air, water, co2 in geothermal production wells. *International Journal of Heat and Mass Transfer*, 132:249–258.

Pope, S. B. and Pope, S. B. (2000). *Turbulent flows*. Cambridge university press.

Prandtl, L. (1952). *Essentials of fluid dynamics: With applications to hydraulics aeronautics, meteorology, and other subjects*. Hafner Publishing Company.

Prasad, B. and Saini, J. (1988). Effect of artificial roughness on heat transfer and friction factor in a solar air heater. *Solar energy*, 41(6):555–560.

Promthaisong, P., Jedsadaratanachai, W., and Eiamsa-Ard, S. (2016). 3d numerical study on the flow topology and heat transfer characteristics of turbulent forced convection in spirally corrugated tube. *Numerical Heat Transfer, Part A: Applications*, 69(6):607–629.

Promvonge, P. and Kwankaomeng, S. (2010). Periodic laminar flow and heat transfer in a channel with 45 staggered v-baffles. *International Communications in Heat and Mass Transfer*, 37(7):841–849.

Promvonge, P. and Thianpong, C. (2008). Thermal performance assessment of turbulent channel flows over different shaped ribs. *International Communications in Heat and Mass Transfer*, 35(10):1327–1334.

Ramgadia, A. G. and Saha, A. K. (2013). Three-dimensional numerical study of turbulent flow and heat transfer in a wavy-walled duct. *International Journal of Heat and Mass Transfer*, 67:98–117.

Rastegari, A. and Akhavan, R. (2018). The common mechanism of turbulent skin-friction drag reduction with superhydrophobic longitudinal microgrooves and riblets. *Journal of Fluid Mechanics*, 838:68–104.

Reynolds, O. (1901). On the extent and action of the heating surface of steam boilers. *Papers on Mechanical and Physical subjects*, page 81.

Robinson, S. K. (1991). Coherent motions in the turbulent boundary layer. *Annual review of fluid mechanics*, 23(1):601–639.

Rodi, W. and Scheuerer, G. (1986). Scrutinizing the k-ε turbulence model under adverse pressure gradient conditions.

Rothstein, J. P. (2010). Slip on superhydrophobic surfaces. *Annual review of fluid mechanics*, 42:89–109.

Saffman, P. and Wilcox, D. (1974). Turbulence-model predictions for turbulent boundary layers. *AIAA journal*, 12(4):541–546.

Saffman, P. G. (1970). A model for inhomogeneous turbulent flow. *Proceedings of the Royal Society of London. A. Mathematical and Physical Sciences*, 317(1530):417–433.

Sawin, J. L., Sverrisson, F., Seyboth, K., Adib, R., Murdock, H. E., Lins, C., Edwards, I., Hullin, M., Nguyen, L. H., Prillianto, S. S., et al. (2016). Renewables 2017 global status report.

Schellenberger, F., Encinas, N., Vollmer, D., and Butt, H.-J. (2016). How water advances on superhydrophobic surfaces. *Physical review letters*, 116(9):096101.

Schoppa, W. and Hussain, F. (1998). A large-scale control strategy for drag reduction in turbulent boundary layers. *Physics of Fluids*, 10(5):1049–1051.

Siddiqui, M. K. et al. (2007). Heat transfer augmentation in a heat exchanger tube using a baffle. *International Journal of Heat and Fluid Flow*, 28(2):318–328.

Singh, S., Singh, B., Hans, V., and Gill, R. (2015). Cfd (computational fluid dynamics) investigation on nusselt number and friction factor of solar air heater duct roughened with non-uniform cross-section transverse rib. *Energy*, 84:509–517.

Smits, A., Ding, L., and Van Buren, T. (2019). Flow over a square bar roughness. In *Proceedings of Turbulence and Shear Flow Phenomena*, volume 11.

Smits, A. J., Young, S., and Bradshaw, P. (1979). The effect of short regions of high surface curvature on turbulent boundary layers. *Journal of fluid mechanics*, 94(2):209–242.

Soltani, M., Kashkooli, F. M., Dehghani-Sanij, A., Kazemi, A., Bordbar, N., Farshchi, M., Elmi, M., Gharali, K., and Dusseault, M. B. (2019). A comprehensive study of geothermal heating and cooling systems. *Sustainable Cities and Society*, 44:793–818.

Spalart, P. R. and McLean, J. D. (2011). Drag reduction: enticing turbulence, and then an industry. *Philosophical Transactions of the Royal Society A: Mathematical, Physical and Engineering Sciences*, 369(1940):1556–1569.

Stalio, E. and Nobile, E. (2003). Direct numerical simulation of heat transfer over riblets. *International Journal of Heat and Fluid Flow*, 24(3):356–371.

Sundén, B. (2012). *Introduction to heat transfer*. Wit Press.

Tanda, G. (2004). Heat transfer in rectangular channels with transverse and v-shaped broken ribs. *International Journal of Heat and Mass Transfer*, 47(2):229–243.

Tandiroglu, A. and Ayhan, T. (2006). Energy dissipation analysis of transient heat transfer for turbulent flow in a circular tube with baffle inserts. *Applied thermal engineering*, 26(2-3):178–185.

Tang, X., Dai, X., and Zhu, D. (2015). Experimental and numerical investigation of convective heat transfer and fluid flow in twisted spiral tube. *International Journal of Heat and Mass Transfer*, 90:523–541.

Tester, J. W., Anderson, B. J., Batchelor, A., Blackwell, D., DiPippo, R., Drake, E., Garnish, J., Livesay, B., Moore, M., Nichols, K., et al. (2006). The future of geothermal energy. *Massachusetts Institute of Technology*, 358.

Tiruselvam, R., Chin, W., and Raghavan, V. R. (2012). Double tube heat exchanger with novel enhancement: part ii—single phase convective heat transfer. *Heat and Mass Transfer*, 48(8):1451–1462.

Turnow, J., Kornev, N., Isaev, S., and Hassel, E. (2011). Vortex mechanism of heat transfer enhancement in a channel with spherical and oval dimples. *Heat and mass transfer*, 47(3):301–313.

Van Buren, T., Floryan, D., Ding, L., Hellström, L., and Smits, A. (2020). Turbulent pipe flow response to a step change in surface roughness. *Journal of Fluid Mechanics*, 904.

Van Buren, T., Hellström, L., and Smits, A. (2019). Turbulent pipe flow response to rough-to-smooth step change in roughness: Flow structure. In *Proceedings of Turbulence and Shear Flow Phenomena*, volume 11.

Van Buren, T., Hellstrom, L. H., Marusic, I., and Smits, A. J. (2017). Turbulent pipe flow response to wall changes targeting specific azimuthal modes. In *Tenth International Symposium on Turbulence and Shear Flow Phenomena*. Begel House Inc.

Vold, M. (2017). Three-dimensional numerical modeling of water flow in a rock-blasted tunnel. Master's thesis, NTNU.

Waleffe, F. (1997). On a self-sustaining process in shear flows. *Physics of Fluids*, 9(4):883–900.

Walsh, M. (1982). Turbulent boundary layer drag reduction using riblets. In *20th aerospace sciences meeting*, page 169.

Walsh, M. J. (1980). Drag characteristics of v-groove and transverse curvature riblets. In *Symposium on Viscous flow drag reduction*.

Wang, G. and Vanka, S. (1995). Convective heat transfer in periodic wavy passages. *International Journal of Heat and Mass Transfer*, 38(17):3219–3230.

Wang, J. (2021). Energy recovery from oil sands reservoirs.

Wang, Z., Koratkar, N., Ci, L., and Ajayan, P. (2007). Combined micro-/nanoscale surface roughness for enhanced hydrophobic stability in carbon nanotube arrays. *Applied physics letters*, 90(14):143117.

WEC, S. (2007). Survey of energy resources 2007. *World Energy Council*.

Wei, C., Nawaz, A., Nath, D., Zirrahi, M., and Hassanzadeh, H. (2022). Subsurface waste heat recovery from the abandoned steam assisted gravity drainage (sagd) operations. *Energy*, 256:124615.

Weihing, P., Younis, B., and Weigand, B. (2014). Heat transfer enhancement in a ribbed channel: Development of turbulence closures. *International Journal of Heat and Mass Transfer*, 76:509–522.

Whalley, R. D. and Choi, K.-S. (2014). Turbulent boundary-layer control with plasma spanwise travelling waves. *Experiments in Fluids*, 55(8):1–16.

White, F. M. and Majdalani, J. (2006). *Viscous fluid flow*, volume 3. McGraw-Hill New York.

Wilcox, D. C. (1993). Comparison of two-equation turbulence models for boundary layers with pressure gradient. *AIAA journal*, 31(8):1414–1421.

Wolf, C., Klein, D., Richter, K., and Weber-Blaschke, G. (2016). Environmental effects of shifts in a regional heating mix through variations in the utilization of solid biofuels. *Journal of Environmental Management*, 177:177–191.

Xu, R., Zhang, L., Zhang, F., and Jiang, P. (2015). A review on heat transfer and energy conversion in the enhanced geothermal systems with water/co2 as working fluid. *International Journal of Energy Research*, 39(13):1722–1741.

Yamagata, T., Ito, A., Sato, Y., and Fujisawa, N. (2014). Experimental and numerical studies on mass transfer characteristics behind an orifice in a circular pipe for application to pipe-wall thinning. *Experimental thermal and fluid science*, 52:239–247.

Yang, L., Du, K., and Zhang, Z. (2020). Heat transfer and flow optimization of a novel sinusoidal minitube filled with non-newtonian sic/eg-water nanofluids. *International Journal of Mechanical Sciences*, 168:105310.

Zagarola, M. V. and Smits, A. J. (1998). Mean-flow scaling of turbulent pipe flow. *Journal of Fluid Mechanics*, 373:33–79.

Zambaux, J.-A., Harion, J.-L., Russeil, S., and Bouvier, P. (2015). The effect of successive alternating wall deformation on the performance of an annular heat exchanger. *Applied Thermal Engineering*, 90:286–295.

Zheng, N., Liu, P., Shan, F., Liu, Z., and Liu, W. (2016). Heat transfer enhancement in a novel internally grooved tube by generating longitudinal swirl flows with multi-vortexes. *Applied Thermal Engineering*, 95:421–432.

Zheng, N., Liu, P., Shan, F., Liu, Z., and Liu, W. (2017). Turbulent flow and heat transfer enhancement in a heat exchanger tube fitted with novel discrete inclined grooves. *International Journal of Thermal Sciences*, 111:289–300.

Zheng, N., Liu, W., Liu, Z., Liu, P., and Shan, F. (2015). A numerical study on heat transfer enhancement and the flow structure in a heat exchanger tube with discrete double inclined ribs. *Applied Thermal Engineering*, 90:232–241.